IEEE Access
Multidisciplinary | Rapid Review | Open Access Journal

Received January 13, 2020, accepted February 16, 2020, date of publication March 2, 2020, date of current version March 12, 2020.

Digital Object Identifier 10.1109/ACCESS.2020.2977842

Onboard Spectral Analysis for Low-Complexity IoT Devices

SIMONE GRIMALDI[1], (Member, IEEE), LUKAS MARTENVORMFELDE[2], AAMIR MAHMOOD[1], (Senior Member, IEEE), AND MIKAEL GIDLUND[1], (Senior Member, IEEE)

[1]Department of Information Systems and Technology, Mid Sweden University, 851 70 Sundsvall, Sweden
[2]Institute Industrial IT-inIT, Technische Hochschule Ostwestfalen-Lippe, 32657 Lemgo, Germany

Corresponding author: Simone Grimaldi (simone.grimaldi@miun.se)

This work was supported by the Swedish Knowledge Foundation (KKS) under Grants 20180170, 20180178, and by the Swedish Foundation for Strategic Research (SSF) under Grant SM18-0044.

ABSTRACT The lack of coordinated spectrum access for IoT wireless technologies in unlicensed bands creates inefficient spectrum usage and poses growing concerns in several IoT applications. Spectrum awareness becomes then crucial, especially in the presence of strict quality-of-service (QoS) requirements and mission-critical communication. In this work, we propose a lightweight spectral analysis framework designed for strongly resource-constrained devices, which are the norm in IoT deployments. The proposed solution enables model-based reconstruction of the spectrum of single radio-bursts entirely onboard without DFT processing. The spectrum sampling exploits pattern-based frequency sweeping, which enables the spectral analysis of short radio-bursts while minimizing the sampling error induced by non-ideal sensing hardware. We carry out an analysis of the properties of such sweeping patterns, derive useful theoretical error bounds, and explain how to design optimal patterns for radio front-ends with different characteristics. The experimental campaign shows that the proposed solution enables the estimation of central frequency, bandwidth, and spectral shape of signals at runtime by using a strongly hardware-limited radio platform. Finally, we test the potential of the proposed solution in combination with a proactive blacklisting scheme, allowing a substantial improvement in real-time QoS of a radio link under interference.

INDEX TERMS Central frequency estimation, cognitive radio, dynamic spectrum access, interference, Internet-of-Things, jamming, spectral analysis, spectrum sensing, unlicensed bands, wireless coexistence.

I. INTRODUCTION

Radio-frequency (RF) communication over industrial, scientific, and medical (ISM) unlicensed bands is a pivotal element of the Internet-of-things (IoT). The last two decades have witnessed the release and evolution of wireless technologies over ISM-bands, such as IEEE 802.11, IEEE 802.15.4, and IEEE 802.15.1, which have *de facto* triggered a massive shift towards the IoT paradigm in countless applications and domains [1]. While the share of IoT applications migrating to a licensed spectrum is expected to increase with the advent of 5G standard [2], ISM-bands-based solutions are expected to remain the first choice for many applications requiring short-range communication [3], thanks to low to non-existent deployment costs and worldwide applicability [4]. The main drawback is that the unlicensed spectrum is already scarce due to multiple technologies competing over overlapping channels and mutually jeopardizing communication quality [5]. Besides, additional interference can be caused by electrical equipment [6] or deliberate RF jamming [7]. Apart from a few proprietary solutions [8], there is a lack of mechanisms for intra-technology spectrum management and medium-access coordination [9]. Moreover, today's IoT wireless devices do not decode, or analyze the properties of signals from other technologies but pursue interference mitigation via threshold-based energy-sensing [10], and *a posteriori* channel-quality evaluation [11] only. The consequence of an inadequate interference mitigation strategy is error-prone communication, which leads to reduced performance guarantees. Such a scenario is critical for applications with strict quality-of-service (QoS) requirements, which are common in the Industrial IoT (IIoT) domain [12]. However, the relevance of the problem is also escalating for applications with more relaxed QoS, e.g., building automation, due to

The associate editor coordinating the review of this manuscript and approving it for publication was Maurizio Magarini.

massive deployment of IoT devices. As both the research community and the standardization groups [13] have identified the issue, several solutions have been proposed [14] to augment and exploit radio-resource awareness in ISM-bands by spectral monitoring [15] and signal classification [16]. The critical insight is that the more profound is the knowledge of the nature and dynamics of interference in time, frequency, and space, the more efficient and adaptive the resource allocation can become. Spectrum scanning and analysis is a master tool in this sense, as it reveals both the allocation and the spectral footprint of RF signals. The consequent spectrum-awareness paves the way for the employment of elaborate approaches such as white-space prediction and dynamic spectrum access [17], which are gaining momentum as the interference level in ISM-bands escalates.

While the market offers some miniaturized spectrum monitoring solutions [18], they mainly perform a relatively slow frequency sweep over large bands, and their target use-case is limited to manual network troubleshooting. As it is not trivial to integrate such solutions with existing low-complexity (LC) IoT (LC-IoT) devices [19], a common workaround is to rely on software-defined radio (SDR)-based analysis [20]. On the other hand, a fully onboard solution that ensures compatibility with existing LC-IoT platforms is a more appealing and cost-effective alternative for IoT applications. Unfortunately, most solutions in the literature seem unsuitable for the LC-IoT devices as they present at least one of the following caveats: i) the required sampling rate and/or memory consumption exceed the specifications, and ii) the required sensing and/or processing time are too long for IoT-network requirements. These points constitute the primary motivation for this work, which presents a comprehensive and lightweight framework for onboard spectrum sensing and analysis. The proposed solution employs detection, sensing, and model-based spectrum reconstruction of single signal-bursts, and it is designed to accommodate platforms with different radio and processing capabilities. Experimental tests performed with TelosB motes (a 15-year-old platform) give baseline performance results as a guarantee of extremely low hardware requirements. This work claims the following scientific contributions:

1) the first approach of its kind extending the capabilities of LC-IoT hardware to the edge of real-time spectrum analysis with burst-based spectrum reconstruction.
2) a thorough analysis of the error properties and optimization of the intra-burst sampling patterns with guidelines on how to extend the results to a wide range of radio platforms.
3) the theoretical study of the performance of the sub-system used for central frequency estimation and its empirical validation via measurement campaign.
4) key-insights on the implementation of an elaborate sampling-and-estimation machine on IoT platforms with extreme constraints on radio and processing capability.
5) real-world tests on the accuracy of the proposed solution with RF signals of various modulations and bandwidths.
6) a use-case showing that the proposed method significantly increases the QoS of ISA100.11a-compliant [11] time-slotted channel-hopping (TSCH) under severe RF interference.

We organize the remainder of the work as follows. Section II gives an overview of coexistence in unlicensed bands and spectrum analysis, while Section III sketches the proposed method. Section IV discusses the spectrum sampling mechanism and its properties, and Section V explains the spectrum reconstruction approach and derives estimation bounds. Section VI tests the accuracy of spectrum reconstruction, while Section VII presents a real-world use-case of the developed solution. Finally, Section VIII summarizes the conclusions.

II. BACKGROUND

Numerous IoT short-range communication systems operate in the 2.4 GHz ISM-band, exploiting an 85 MHz-wide unlicensed spectrum. The lack of a common coexistence framework that coordinates the time and spectrum usage among different IoT technologies is a well-documented issue and has stimulated many approaches in the literature.

A. COGNITIVE RADIO METHODS

A cognitive radio (CR) is a radio system that can acquire information on the radio environment and adapt its operating parameters accordingly [14]. The CR approach was introduced to enable opportunistic transmission of license-exempt devices (secondary users) over licensed bands [21]. At the same time, CR is particularly relevant to coexistence in overcrowded unlicensed bands, where cross-technology coordination is often absent, and the wireless networks show mutual interference-like disruptive effects. A critical aspect of CR is the design of the spectrum scanning mechanism used to reveal the presence of primary users (licensed devices) and determine their spectral occupancy. For example, [22] discusses the timing of the spectrum scanning under ON/OFF interference models with different arrival/idle-time distributions, while the use of maximum-likelihood and Bayesian inference in this context is proposed in [23]. The optimization of the scanning process under the assumption of an ON/OFF interference model is also studied in [22] and [23]. The primary/secondary user approach of such works encompasses signal detection but not signal analysis, meaning that the spectral features of the signal are not estimated. Moreover, the detection-only approach becomes limiting when the primary user technologies are many, and their spectral allocation and spectral footprint is diverse, which is the case of IoT in unlicensed bands. For this reason, several methods have been proposed that target the classification of the interference in a supervised [24], [25] or unsupervised (model-based) fashion [26].

B. CHANNEL ADAPTATION IN IIoT STANDARDS

Despite the availability of several CR mechanisms, the wireless standards for IoT have not yet embraced the approach and rely instead on basic or naive coexistence techniques. Notable examples are the IEEE 802.15.4-based IIoT standards, such as WirelessHART, ISA 100.11a, and WIA-PA, which are widely used for closed-loop control and monitoring applications. The standards commonly provide a frequency-diversity mechanism via TSCH, to counterbalance communication performance drop in moderately interfered environments (e.g., coexistence with IEEE 802.11 WLANs [27]). In particular, the ISA100.11a standard includes different frequency hopping patterns and an optional spectrum management mechanism with a-posteriori channel blacklisting. The mechanism periodically monitors channel-specific metrics and blacklists the channels exhibiting poor properties (i.e., shortens the hopping-sequence). The approach, like others in the literature [28], [29], provides a channel selection policy that maximizes packet delivery ratio in the long term, but that is not ideal for time-critical communication [30], where QoS requirements encompass a time-horizon of few transmissions. It means that a sudden quality-drop on multiple channels can rapidly cause a radio-link blackout [31] without leaving enough time for a measure-and-adapt mechanism to operate.

C. FUNDAMENTALS OF SPECTRUM ANALYSIS

Spectral analysis of RF signals is possible through several approaches. We briefly overview the two architectures that are more relevant to contextualize the solution presented in this work, while we remind to specific literature for further details [32].

The most straightforward and traditional architecture is the superheterodyne or swept-tuned spectrum analyzer (SSA) shown in Fig. 1a. The SSA carries out spectrum analysis by sweeping the downconverted version of the signal through a band-pass filter (BPF) and measuring its output for different frequency bins. The performance of SSAs is affected by the BPF-bandwidth, called resolution-bandwidth (RBW), as a narrow RBW increases the resolution of the analysis at the cost of longer sweep time, hindering the analysis of short bursty signals. Modern solutions [33] employ a different architecture with a DSP-based real-time spectrum analysis that enables higher frequency-resolution and processing speed, allowing to profile bursty signals of sub-µs duration [32]. The operating principle is represented in Fig. 1b, and bases on the fast Fourier transform (FFT) of the signal after downconversion. The capture bandwidth, in this case, is limited by the Nyquist frequency, meaning that a sampling rate exceeding twice the bandwidth of the analyzed signal is required. Moreover, to extract the spectrogram of short radio bursts, multiple FFT operations need to be performed within the duration of the burst [32], which escalates sample rate and hardware requirements. While the real-time analysis needs powerful dedicated platforms, we show how the SSA-inspired architecture in Fig. 1c applied to single signal

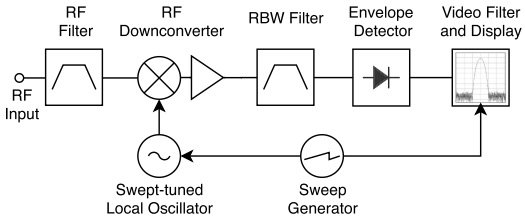

(a) Swept-tuned spectrum analyzer (SSA).

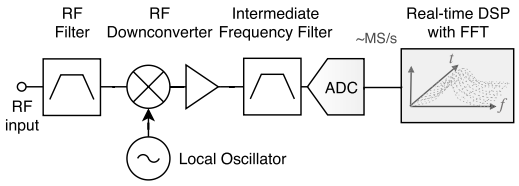

(b) Real-time spectrum analyzer.

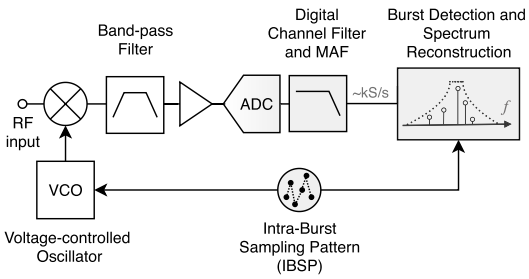

(c) The employed approach to burst-based spectrum sampling with embedded IoT platforms.

FIGURE 1. Simplified block diagrams of different architectures for spectrum analysis. The blocks operating digital processing are represented in gray.

bursts is a key component to realize a fully onboard spectrum analysis solution for LC-IoT hardware. We present such a solution in Section III and Section IV.

D. CHALLENGES OF SPECTRUM ESTIMATION WITH IoT HARDWARE

The FFT-based spectrum analysis is the leading approach in the related literature. Unfortunately, such a method collides with the characteristics of LC-IoT devices in many ways. First, the Nyquist theorem poses a tight requirement on the sampling rate, which means, e.g., at least 40 MS/s for profiling IEEE 802.11 signals. It translates into an instantaneous bandwidth that is unrealistic for LC-IoT devices. Moreover, the presence of other in-band emissions, such as jamming devices [7], [34], or wideband RF noise (e.g., microwave ovens [6]) further complicates the definition of sampling requirements. Finally, computing the FFT for the detected bursts is a time- and memory-consuming task for embedded hardware and workarounds are needed. For example, the computation of FFT in the presence of incomplete sampling is discussed in [35]. The approach is formalized in the compressive sensing framework (see [36] and references therein), which allows the reconstruction of the signal spectrum from incomplete and sub-Nyquist sampling. The price

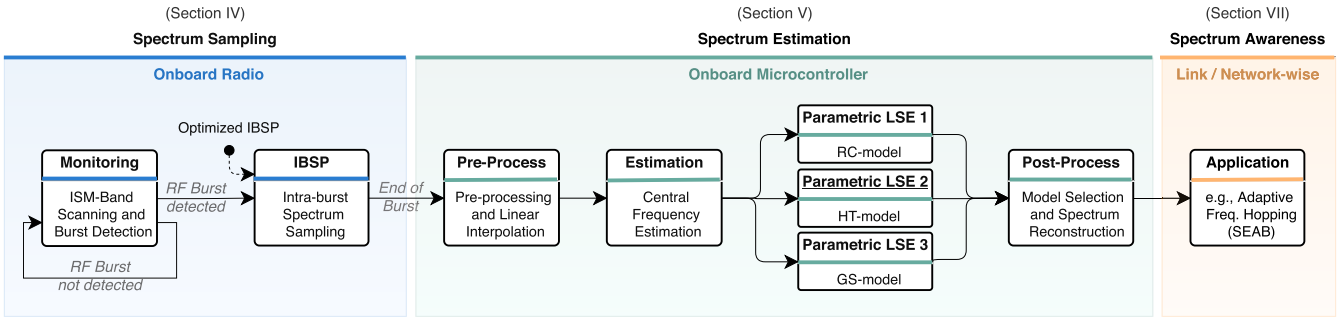

FIGURE 2. Overview of the proposed approach to burst-based spectral analysis together with the examined dynamic spectrum access application.

to pay for this approach is an increased computational complexity w.r.t. FFT alone, which makes the method unsuitable for LC-IoT platforms.

Another notable obstacle to onboard spectral analysis is the acquisition of RF signals at the radio interface. Most radio platforms only provide measurements of the RF power through the received signal strength indicator (RSSI) [37], which is a heavily pre-processed and real-valued version of the raw I/Q data handled internally by the radio chip. The RSSI samples are usually the result of both channel- and moving-average-filtering (MAF) that has a significant low-pass filter effect and introduces sample-correlation. The MAF is especially problematic since it removes the super-kHz frequency content and renders FFT-based analysis worthless. Moreover, the onboard microcontroller limits the RSSI sampling rate, which can be orders of magnitude lower than the Nyquist-rate. All these effects make burst-based FFT analysis impossible with most LC-IoT platforms. In this paper, we show instead that an alternative solution is possible by embracing an optimized SSA empowered by central frequency estimation and spectrum reconstruction.

III. OVERVIEW OF THE PROPOSED SOLUTION

This section gives a brief overview of the different modules of the system proposed in Fig. 2. It also sketches minimum hardware requirements for the target IoT platforms. Later, Sections IV and V provide exhaustive description of the intra-burst sampling and the spectrum reconstruction modules.

A. GLOBAL SCANNING AND BURST DETECTION

The first component of the solution in Fig. 2 provides global spectral scanning and burst-detection capabilities. The detector reveals the initial transient of radio-bursts following a non-coherent threshold-based approach. The scanning process can target any spectral region within the ISM-band and continuously scrutinizes the energy samples available with the specific platform (e.g., IEEE 802.15.4-compliant RSSI samples). For minimizing the false-positive detection, each device performs a quick radio-calibration [38] during the booting process, profiles the noise-floor at its radio interface, and adapts the detection-threshold accordingly.

B. INTRA-BURST SPECTRUM SAMPLING

When the burst detector is positive, the intra-burst sampling system is activated (IBSP-block of Fig. 2). The system operates as the SSA described in Section II, with the notable difference that the frequency sweep is not linear but follows a pre-calculated intra-burst sampling pattern (IBSP), as represented in Fig. 1c. The choice is due to the limited sampling rate achievable with LC-IoT radios compared to the typical duration of radio bursts. A linear IBSP would have a small chance of being completed within the radio-burst lifetime, potentially leading to vast unexplored regions of the signal spectrum. Instead, the proposed system acquires sparse frequency samples and then relies on matched spectral models to estimate the spectral shape. The problems that such a system addresses are a consistent measurement error due to time- frequency-correlation of samples, slow stabilization of frequency synthesis circuit, and limited sampling rate. Our model in Section IV takes into account these non-idealities allowing the optimization of the IBSP for different LC-IoT platforms.

Example requirements: i) Sampling of the RF signal at the radio interface with a rate of at least[1] *10kS/s, ii) availability of samples before full stabilization of the onboard frequency synthesizer.*

C. SPECTRUM ESTIMATION

As the burst detection system signals the end of the radio-burst, the frequency samples are rearranged and sent to the spectrum reconstruction module. The module employs three parametric spectrum models, where the parameters are sequentially fitted using a greedy-algorithm for mean squared error (MSE)-minimization. The estimation of the central frequency is based instead on a specific estimator, which we study separately in Section V-C. The model with the lowest MSE is then chosen as a spectral estimate, and spectral parameters (e.g., bandwidth) are extracted. The analysis is operated in real-time, and the spectral estimate is available after platform-dependent processing time. To keep the method implementable on a broad set of LC-IoT platforms,

[1]It allows the spectral analysis of radio bursts with a minimum duration of $\approx 400\,\mu$s over a 50 MHz band (see Section VI).

we have designed a modular structure where the number and complexity of spectral models can be adapted. Furthermore, we have included a fallback method in the form of linear interpolation (LI), providing a parameter-fitting-free reconstruction method for platforms with extreme constraints.

Example requirements: i) onboard microcontroller allowing LI in real-time of $\approx$ 50 – *8bit-samples. ii) optionally, non-linear model fitting with parameter space of size in the order of magnitude of* $\approx 10^3$ *points.*

D. SPECTRUM AWARENESS

The real-time estimation of signal spectrum *de facto* opens interesting possibilities for CR applications, such as dynamic spectrum access for low-power devices. While a comprehensive discussion on the potential use of the spectral information falls outside the scope of this work, we show how the proposed solution can be used to enhance the reliability of an ISA100.11a radio link under interference (see Section VII).

IV. INTRA-BURST SPECTRUM SAMPLING

Swept-spectrum sampling with commodity radio front-ends is slow and error-prone, and specific intra-burst sampling patterns (IBSPs) are needed to ensure acceptable performance. In this section, we define a rationale for finding patterns that optimize the sampling process affected by measurement errors, sample-correlation, and incomplete sampling.

A. DEFINITION AND NUMERICAL PROPERTIES OF IBSPS

The (l, k)-IBSPs are here formally introduced, and later some baseline properties are derived.

Definition 1: A (l, k)*-IBSP* S *is a* l*-tuple* $\{s_0, s_1, \ldots, s_{l-1}\}$ *where each element* $s_n \in \mathbb{Z}$ *verifies* $|s_n| \leq k,\ \forall n \in [0, l-1]$ *with* $k \in \mathbb{N}$, $k \geq 1$.

Definition 2: A (l, k)*-IBSP* S *is said to be complete if it is a permutation of the* $(2k+1)$*-tuple* $\{-k, -k+1, \ldots, 0, \ldots, k-1, k\}$.

The elements of the IBSP are the frequency-offsets which guide the radio front-end in the process of sampling the spectrum of the radio burst. Specifically, the IBSP element s_i maps onto the actual frequency value $f_{s_i} = f_I + \delta_f s_i$, where f_I is the center of the IBSP (e.g., the index $s_i = 0$) and δ_f is the granularity of frequency selection. For example, it is $\delta_f = 1$ MHz for the platform considered in this work. When $l = 2k+1$, the IBSP allows the collection of the maximum number of unique frequency samples over the $\delta_f(2k+1)$-MHz-wide frequency region. The following lemma clarifies the cardinality of complete (l, k)-IBSP sets.

Lemma 1: The set of all (l, k)*-IBSPs,* $\mathcal{S}_{l,k}$ *has cardinality* $(2k+1)^l$*, while the subset* $\mathcal{C}_{l,k} \subseteq \mathcal{S}_{l,k}$ *of* (l, k)*-IBSPs that are also complete has cardinality* $(2k+1)!$.

Proof: See Appendix A. □

Lemma 1 arises from basic combinatorics and shows that even the subset of complete-IBSPs is extremely numerous. For example, the exploration of a 51 MHz band with 1 MHz granularity and a (51, 25)-complete-IBSP implies a selection within a set of $\approx 1.5 \times 10^{66}$ IBSPs. The subsequent step is the introduction of a sampling-error model so that the selection of IBSP can be adequately formulated as a minimization problem within the $\mathcal{C}_{l,k}$ set, which ultimately points to IBSPs with desirable error properties.

B. EFFECTS OF NON-IDEAL SAMPLING–THE ERROR MODEL

High sampling rate and fast frequency switching are favorable points for executing IBSPs. Anyway, as discussed in Section II-D, LC-IoT front-ends fall short on these requirements, and usually add other non-idealities leading to sub-optimal sampling, which are 1) temporal correlation among samples (RSSI filtering) 2) uncertainty in the sample value, 3) constrained RBW, and 4) inaccurate frequency selection. We examine these effects separately.

1) TIME-CORRELATION

Given the time-window T_c of a MAF with uniform weighting coefficients, we introduce $F(t)$, $t \geq 0$, as the cumulative distribution of the MAF weights. Then, it is $F(t) = t/T_c$ for $0 \leq t \leq T_c$, and $F(t) = 1$ for $t > T_c$. Let us consider a sample acquired at the sampling instant $t_i = t_0 + iT_s$, with T_s IBSP sampling period and t_0 initial time. Then, the correlation function $C(t_i - t_{i-j}) = 1 - F(t_i - t_{i-j})$ quantifies the influence of the sample with index $i-j$ on the current sample i. If the IBSP sampling rate is higher than the rate of the filtering process, i.e., $T_s < T_c$, at least one of the previous samples is correlated with the current one. The cumulative effect of previous samples is given by $\sum_{i=1}^{L_c} C(iT_s)$, where $L_c \in \mathbb{N}$ is the highest integer such that $L_c T_s \leq T_c$ and represents the number of past samples contributing to the correlation. Based on this model, we define E_C as the component of the IBSP-sampling error due to the MAF. In particular, E_C describes the error level carried by a generic spectral-sample, s_i, of the IBSP S, when sampling the power spectral density (PSD) $X(f)$ centered around f_c. It is

$$E_C(i) = \sum_{j=1}^{L_c} C(jT_s)\, D(s_i, s_{i-j}), \tag{1}$$

where $D(s_i, s_{i-j}) \triangleq |X(f_\Delta + s_i\delta_f) - X(f_\Delta + s_{i-j}\delta_f)|$ is the spectral distance calculated as the difference of the PSD at the frequencies pointed by the IBSP elements s_i and s_{i-j}, $f_\Delta = f_c - f_I$ is the frequency offset between the signal and the IBSP center, and $D(s_i, s_{i-j}) = 0$ if $j > i$. In practice, the higher is the difference between the PSD value of correlated-samples, the higher the sampling error. An interesting effect of the time-correlation is that, as the sampling rate increases, the number of correlated samples (L_c) increases, and the error component E_C grows. Hence, the model suggests that over a certain sampling rate, the gain of having more samples is progressively nullified by the MAF error.

2) ADDITIVE NOISE

The second component of the error function is an additive white Gaussian noise (AWGN) process $n(i)$ of variance σ_N^2,

which models the uncertainty on the measurement of each sample due to platform's intrinsic accuracy. The value is customarily reported by RF chip vendors in the form of RSSI accuracy or can easily be determined with calibration [38].

3) CHANNEL FILTERING

The RF signal is commonly pre-processed with a digital channel filter [39] (see Fig. 1c), where the filter-bandwidth reflects the PHY specifications (e.g., adjacent-channel rejection) of the implemented standard. Albeit the filter does not introduce sampling errors in the strict sense, it constrains the RBW, which leads to a correlation between spectral samples closely spaced in frequency. We model this correlation by means of the normalized auto-convolution $R_H(f) = H_c(f) \circledast H_c(f)$, with $H_c(f)$ the frequency response of the channel filter. Then, the measurement system introduces no frequency-correlation in IBSP samples spaced at least B_c-MHz, with B_c the width of the support of $H_c(f)$.

4) VCO STABILIZATION

As the IBSP sampling rate can be particularly demanding, the circuitry employed for frequency regulation might not be fast enough to correctly stabilize the output of the onboard voltage-controlled oscillator (VCO) between consecutive spectral samples (see [39]). The effect is that a sample might be acquired on an inaccurate frequency, leading to measurement errors. A common solution in embedded-platforms is the use of a VCO in a phase-locked loop (PLL) configuration. For this reason, we use the second-order PLL transient-state model in [40] for expressing the evolution of the frequency selection error e_V during the transition from frequency f_{i-1} to f_i as $e_V(t) = |f_i - f_{i-1}| k_n t e^{-\omega_n t}$, $t \geq 0$; ω_n is the natural frequency of the PLL, depending on the specific circuit-design and k_n is a normalization constant such that $k_n t e^{-\omega_n t} \leq 1$. We then assume that the resulting sampling-error component $E_V(i)$ is linearly related to $e_V(t)$ with angular coefficient given by the spectral distance $D(s_i, s_{i-1})$, hence

$$E_V(i) = D(s_i, s_{i-1}) |f_{s_i} - f_{s_{i-1}}| k_n T_s e^{-\omega_n T_s}, \tag{2}$$

since the exponential term is always calculated in the sampling instants, which are periodic with T_s.

5) AGGREGATE MODEL

Under this assumption, it is possible to write the total error of a IBSP sample i as

$$\begin{aligned} &E(i) \\ &= E_C(i) + E_V(i) + n(i) \\ &= \sum_{j=1}^{L_c} C(jT_s)\, D(s_i, s_{i-j}) + D(s_i, s_{i-1}) |f_{s_i} - f_{s_{i-1}}| g_V(T_s) + n(i), \end{aligned} \tag{3}$$

where we let $g_V(T_s) \triangleq k_n T_s e^{-\omega_n T_s}$. Hence, $E(i)$ is a random vector with mean $\mu_i = E_C(i) + E_V(i)$ and variance $\sigma_i^2 = \sigma_N^2$. Since both (1) and (2) depend on the spectral distance $D(s_i, s_j)$, it follows that a model of the observed spectrum is needed to derive a closed-form expression of the total sampling error $E(i)$. Therefore, we make the simplifying assumption that the difference $D(s_i, s_j)$ varies linearly with the spectral distance i.e., $D(s_i, s_j) \approx k_f \delta_f |s_i - s_j|$, with k_f regulating the slope of the spectrum model. Under this assumption, (3) simplifies into

$$\begin{aligned} E_{lin}(i) = k_f \delta_f \sum_{j=1}^{L_c} C(jT_s)\, |s_i - s_{i-j}| \\ + k_f \delta_f^2 |s_i - s_{i-1}|^2 g_V(T_s) + n(i). \end{aligned} \tag{4}$$

Finally, the cumulative sampling error $\mathcal{E}_{lin}(S)$ arising from the entire (l, k)-IBSP S, follows from (4) as

$$\begin{aligned} \mathcal{E}_{lin}(S) = k_f \delta_f \Big[\sum_{i=1}^{l-1} \sum_{j=i}^{L_c} C(jT_s)\, |s_i - s_{i-j}| \\ + \delta_f g_V(T_s) \sum_{i=1}^{l-1} |s_i - s_{i-1}|^2 \Big] + \sum_{i=0}^{l-1} n(i), \end{aligned} \tag{5}$$

with the time-correlation and VCO settling errors acting from the sample $i = 1$ collected after the first frequency selection, and with the noise component perturbing all the IBSP samples.

C. FINDING OPTIMAL IBSPS

This section studies the error function in (5) and later designs an optimization problem that takes into account the possibility of incomplete IBSPs due to the physical constraints of the platform and the limited duration of radio-bursts. We begin with the following theorem to provide the lower bound on the cumulative sampling error.

Theorem 1: Let S be a complete (l, k)-IBSP and consider the sample-error model in (5)*, then, if the number of correlated samples is $L_c = 1$ the following bound holds on the cumulative sampling error of S*

$$\mathbf{E}\left[\mathcal{E}_{lin}(S)\right] \geq (l-1)\, k_f \delta_f\ e_p(T_s), \tag{6}$$

with $e_p(T_s) \triangleq C(T_s) + k_n \delta_f T_s e^{-\omega_n T_s}$ the sampling error induced by the previous IBSP sample.

Proof: See Appendix B. □

Corollary 1: Let S be a linear (l, k)-IBSP constructed as $S_{lin} = \{(-l+1)/2, (-l+3)/2, \ldots, (l-1)/2\}$, and let $L_c \leq 1$, then both S_{lin} and its reverse S'_{lin} are complete (l, k)-IBSPs and attain the mean sampling error bound in (6) *with equality sign.*

Proof: See Appendix C. □

Theorem 1 and its corollary prove that linear IBSPs are an optimal choice w.r.t. the sampling error, while (5) gives a practical method for its estimation. Unfortunately, linear IBSPs are of limited interest in real-world implementations, since they explore the target spectral region slowly and might hinder the spectrum estimation when only a few samples are available (short-bursts/slow-sampling). Such a problem loops back into the limitation of SSAs in capturing transient events,

which is described in Section II-C, as linear IBSPs *de facto* realize a burst-based SSA with a discrete frequency sweep. In other words, the truncation of the linear IBSPs might result in a relevant region of the spectrum remaining unobserved, as we verify in Section VI.

D. THE CONSTRAINED IBSP INTEGER PROGRAM

The remainder of this section focuses on finding complete IBSPs with favorable properties, even in the case of incomplete sampling. For this purpose, we target the error function in (5) and formulate the following constrained optimization problem

$$\underset{S}{\text{minimize}}\ \mathcal{E}_{lin}(S) \tag{7a}$$

$$\text{subject to:}\ \ s_0 = 0 \tag{7b}$$

$$\sum_{i=0}^{m} f_{s_i} - k_{bal} \ \leq\ 0 \tag{7c}$$

$$\sum_{i=1}^{m}\sum_{j=1}^{i} R_H(f_{s_i} - f_{s_{i-j}}) - k_{cor} \ \leq\ 0, \tag{7d}$$

where the inequality constraints (7b), (7c) and (7d) center the IBSP around the detection frequency f_I and restrict the solution-space to the IBSPs that satisfy both frequency-correlation and sampling-symmetry properties w.r.t their partial IBSP length $m \leq l$. The parameters k_{bal} and k_{cor} are discussed in the following sections.

1) CENTERING IBSP

The element s_0 in (7b) shifts the IBSP center f_I w.r.t the detection frequency, and its selection depends on the assumption on signal spectrum. It is reasonable to assume that the expected value of the detection frequency coincides with the spectral center for symmetric PSD - we justify this idea during the assessment central frequency estimation in Section VI-B. If the assumption is correct, then the choice $s_0 = 0$ guarantees that, on average, the IBSP locks on the spectral center of the signal under analysis, which is the desired property.

2) FREQUENCY-BALANCE

Inequality (7c) ensures that the first m-samples of the IBSP are taken in a balanced manner on the right and the left side of f_I such that the sum of the relative frequency shifts is at most k_{bal}-MHz. This balancing avoids the situation where the first part of the IBSP predominantly explores only one side of the spectrum, potentially leading to inaccurate spectrum reconstruction. The linear IBSPs are the most notable example of unbalanced IBSPs that violate constraint (7c) for a significant span of k_{bal} values.

3) FREQUENCY-CORRELATION

Constraint (7d) considers the RBW of the radio-system and ensures that the total frequency-correlation among the first m-samples is lower than the parameter k_{cor}. As discussed before, a high-RBW induces measurement correlation in closely-spaced spectral samples, which is quantified by the auto-convolution function $R_H(f)$. Thus, this constraint plays an opposite role w.r.t. $\mathcal{E}_{lin}(S)$, since it discards solutions where the first m-samples are densely grouped in certain spectral regions, with parameter k_{cor} tuning the spectral-sparsity of the feasible IBSPs.

TABLE 1. Model parameters of the target platform [39] and setup parameters for the optimization problem.

Parameter	Value	Description
δ_f	1 MHz	Minimum frequency step.
f_n	25 kHz	PLL natural frequency (estim. from T_{VCO}).
T_{VCO}	192 µs	VCO settling-time.
T_c	128 µs	Moving-average filter period.
F_s	9.9 kS/s	IBSP sampling rate.
L_c	1	Number of time-correlated samples.
(l, k)	$(51, 25)$	IBSP length and total span (51 MHz).
k_f	6 dB/MHz	Angular coefficient of spectrum model.
m, k_{cor}, k_{bal}	$k/2$, $0.8 \cdot m$, 1 MHz,	Constraints parameters.

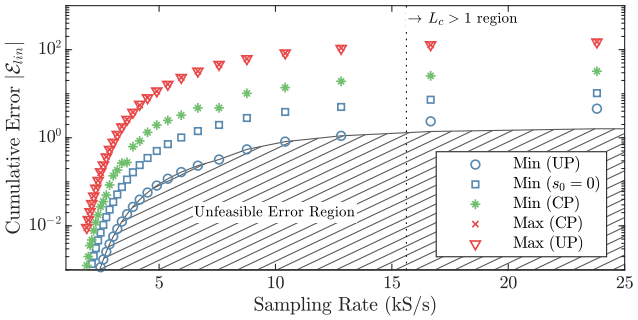

FIGURE 3. Minimum-error solutions of (7) and error-bound (6) vs. IBSP sampling rate for unconstrained problem (UP), fully constrained problem (CP), and constraint (7b) only. The maximum-error solutions are shown as a reference.

E. COMPUTING PLATFORM-SPECIFIC OPTIMIZED IBSPS

The presented optimization problem allows deriving optimized IBSPs for a wide range of devices. The solution of the non-linear integer-program (7) is, in fact, an IBSP tailored to the characteristics of a specific radio front-end through the parameters of the cost function $\mathcal{E}_{lin}(S)$ in (5). Specifically, we target a LC-IoT IEEE 802.15.4 platform and initialize $\mathcal{E}_{lin}(S)$ using the model-parameters reported in Table 1. Problem (7), which is NP-hard [41], is solved via a random-search approach. The linear IBSPs are tested first, to boost convergence-time in case the selection of k_{bal} and k_{cor} allows linear IBSPs as feasible solutions. Fig. 3 shows the feasible minima of the cost function (7) for different sampling rates (i.e., $1/T_s$) when optimizing complete $(51, 25)$-IBSPs for the analysis of a 51 MHz-wide frequency region. The figure also shows the bound (6) and the effect of the three constraints (7b), (7c), and (7d) on the feasible minima. As expected, the unconstrained problem yields linear IBSPs, which exactly matches the lower-bound in the region where the approximation $L_c = 1$ is valid. The inclusion of the three constraints shifts up the minimum considerably, as several IBSPs become unfeasible; yet, it is expected that these IBSPs

provide better sampling performance in real-cases, which we verify in Section VI.

V. SPECTRUM RECONSTRUCTION

This section develops a method for reconstructing the spectral shape, starting from the set of noisy samples collected by the previously described IBSP-based spectrum scanner.

A. PARAMETRIC SPECTRUM MODELING

In order to reconstruct the signal spectrum from the acquired IBSP samples, we introduce a multi-model (MM) parametric reconstruction. The method aims to give a certain degree of flexibility in spectral reconstruction and accommodates several modulated signal formats. In fact, since the nature of the incoming signals is generally unknown, it is challenging to make hypotheses on their PSDs, which suggests the use of comprehensive spectral models. Conversely, the processing limitations of LC-IoT hardware impose constraints on the complexity of the model, suggesting a limited number of parameters to optimize. We thereby describe the chosen models, where $\boldsymbol{\theta}$ is the parameter vector and $\hat{f}_c$ (which is common to all the models) is the estimated central spectral frequency, whose derivation concerns Section V-C.

1) RAISED-COSINE (RC) SPECTRUM

The RC model follows the classic formulation of raised-cosine filters [42] and has parameter vector $\boldsymbol{\theta} = \{\hat{f}_c, \beta, B\}$. Particularly, the roll-off parameter $\beta \in [0, 1]$ controls the slope of the spectral tails and B affects the width of the flat-top part of the spectrum. The introduction of this model originates from the fact that RC-filters are a common choice for the pulse-shaping of modulated signals.

2) HYPERBOLIC-TAILED (HT) SPECTRUM

The HT spectrum model is defined as

$$Y_H(\boldsymbol{\theta}, f) = \begin{cases} 1, & \left|f - \hat{f}_c\right| < \frac{1}{2T} \\ \left(\left|f - \hat{f}_c\right| - \frac{1}{2T} + 1\right)^{-\alpha}, & \text{otherwise,} \end{cases} \tag{8}$$

and $\boldsymbol{\theta} = \{\hat{f}_c, \alpha, T\}$, where the non-negative parameter α controls the spectral decay and T expands and shrinks the flat-top part of the spectrum. The model is inherently similar to the RC (T^{-1} and B have a similar effect) except for the spectral tails, which are entirely convex to accommodate the typical OFDM spectral footprint without relying on more complex models [43].

3) GAUSSIAN SPECTRUM (GS)

The GS model has the simplest formulation and the lowest number of parameters. It is

$$Y_G(\boldsymbol{\theta}, f) = \exp\left(-\frac{(f - \hat{f}_c)^2}{2\sigma}\right), \quad \left|f - \hat{f}_c\right| < B, \tag{9}$$

with $\boldsymbol{\theta} = \{\hat{f}_c, \sigma\}$, where σ regulates the width of the Gaussian bell. The auxiliary parameter B controls the support of the model and does not generally require fitting. The motivation of the GS arises from the need for a long-tailed and non-flat-top spectrum model.

4) LINEAR INTERPOLATION (LI)

The LI method is included as a low-complexity fallback mode. The LI algorithm interpolates the available IBSP-trace to reconstruct missing spectral samples arising from incomplete scanning. Since LI is not a parametric model, it does not need parameters fitting or central frequency estimation; hence, it is expected to be notably faster.

B. PARAMETER ESTIMATION STRATEGY

Considering the non-linearity of the chosen spectrum models, we employ a non-linear least-squares (NLLS) parametric estimation. The general formulation of the estimation problem is

$$\begin{aligned} &\min_{\boldsymbol{\theta}} \sum_{n=0}^{l-1} a_n[\hat{Y}(\boldsymbol{\theta}, f_0 + \delta_f n) - Y(f_0 + \delta_f n)]^2 \\ &\text{s.t. } l_j \le \theta_j \le u_j, \quad \forall j \in [1, M], \end{aligned} \tag{10}$$

where $Y(f)$ is the IBSP-sampled spectrum, $\hat{Y}(\boldsymbol{\theta}, f)$ is the target model to optimize, $\boldsymbol{\theta}$ is the $(M+1)$-parameters vector of the spectrum model, and f_0 is the lowest frequency of the IBSP, i.e., $f_0 = f_I - \delta_f k$ for complete (l, k)-IBSPs. The coefficients a_n are unitary if the sample at frequency $f_0 + \delta_f n$ is acquired and $a_n = 0$ otherwise. Finally, the constraints l_j and u_j are used to restrict the solution-space to physically meaningful parameters, e.g., $\beta \in [0, 1]$ in the RC model. Problem (10) is solved as separate NLLS parametric estimation problems for the different spectrum models. There are several techniques for solving the single NLLS problems, e.g., gradient-methods. Since the algorithm is executed at runtime on resource-constrained embedded platforms, a lightweight and derivative-free method is required. For this reason, we have selected a straightforward alternating-variable optimization, which we describe in Algorithm 1. The proposed optimization is repeated for all the spectral models and the minimum-MSE (MMSE) model $\hat{Y}(\boldsymbol{\theta}^{(opt)}, f)$ is selected in the MM. Although the proposed approach considerably reduces the complexity of the NLLS problem, it requires particular attention to the sequential parameter fitting procedure. Particularly, since the central burst frequency f_c is estimated as the first step, a poor estimator (i.e., a shifted central frequency) could irremediably affect the fitting of the other parameters and severely compromise the accuracy of the reconstructed spectrum. We study this problem in detail in the next section and propose ad hoc methods for estimating f_c.

C. CENTRAL FREQUENCY ESTIMATION

We begin the section by proposing an estimator for f_c and deriving its estimation bias and variance together with the related Cramér-Rao lower bound (CRLB). These analytic insights are used to design four variants of the original estimator of increasing complexity. The candidate estimators

Algorithm 1 Sequential NLLS Algorithm

Load estimated central frequency $\hat{f}_c$; Initialize step vector $\boldsymbol{\delta}_\theta$; set $g(0) = \max$;
for $j := 1$ *to* M **do**
  Initialize parameter $\theta_j^{(1)} = l_j$ in vector $\boldsymbol{\theta}$;
  Initialize $I_{max} \in \mathbb{N}$ s.t. $I_{max} \leq (u_j - l_j)/\delta_{\theta_j}$;
  for $i := 1$ *to* I_{max} **do**
    update parameter vector
    $\boldsymbol{\theta} = (\hat{f}_c, \theta_1, \ldots, \theta_j^{(1)} + (i-1)\delta_{\theta_j}, \ldots, \theta_M)$;
    render model $\hat{Y}(\boldsymbol{\theta}; f)$;
    calculate $g(i) = \mathrm{MSE}[\hat{Y}(\boldsymbol{\theta}; f), Y(f)]$;
    update $\Delta_g(i) = g(i) - g(i-1)$;
    if $\Delta_g(i) > 0$ **then**
      local minimum, save $\theta_j^{(opt)} \leftarrow \theta_j^{(i-1)}$;
      save model MMSE $g(i-1)$;
      break;
    save $\theta_j^{(opt)} \leftarrow \theta_j^{(i)}$;
    save model MMSE $g(i)$;
  end
end

are then implemented in the target LC-IoT platform, and their performance is experimentally assessed and discussed in Section VI. Our mathematical traction has some points of contiguity with the fine frequency estimators analyzed by Jacobsen [44] and references therein, and Candan [45]. Albeit they also target fast frequency estimation, these approaches are based on the discrete Fourier transform and require information on both the magnitude and phase of the measured signals. In contrast, our approach only relies on noisy and often incomplete real-valued samples of the spectral density. We begin by defining a measurement model, which is used throughout the section.

1) SPECTRUM MEASUREMENT MODEL (SM MODEL)

Let $Y[n] = X[n] + N_o[n]$ noisy spectral samples with $N_o[n]$ AWGN noise samples and $n \in \mathbb{N}$ such that $0 \leq n \leq N-1$. The discrete spectrum $X[n]$ represents the local value of the PSD $X(f)$ at the points $f_0 + n\delta_f$, with f_0 the lowest frequency component of the IBSP. Let $X(f)$ be strictly limited within the interval $[f_0, f_0 + \delta_f(N-1)]$ and centered around $f_c = f_0 + m\delta_f$, $m \in \mathbb{N}$, with $0 \leq m \leq N-1$, and $\delta_f \in \mathbb{R}$ frequency granularity.

We introduce now a simple estimator for f_c, and study its mean and variance in the following propositions.

Proposition 1: Given the SM model and the central frequency estimator

$$\hat{f}_c = f_0 + E/S, \tag{11}$$

with $S \triangleq \sum_{n=0}^{N-1} Y[n]$, $E \triangleq \sum_{n=0}^{N-1} n\delta_f Y[n]$. *If* $X(f)$ *is symmetric around* f_c, *the following approximation for the estimation bias holds at the* 5 % *significance level*

$$\mathbf{E}[\hat{f}_c] - f_c \approx \sigma_o^2 N \mu_E / \mu_S^3, \tag{12}$$

if the coefficients of variation (c.v.) satisfy $c.v.(S) \geq 0.005$, $c.v.(E) \leq 0.39$, *with* σ_o^2 *measurement noise variance.*

Proof: See Appendix D. □

Proposition 1 and its proof provide a simple method for constructing a central frequency estimator with controlled bias. It is also evident from (12) that the bias term is governed by the SNR μ_S^2/σ_o^2. It follows that, if the SNR is sufficiently high, the estimation bias tends to zero under three hypothesis: i) the IBSP span is broader than the signal spectrum, ii) the central frequency is one of the scanned bins, and iii) the IBSP is complete and explored in its entirety, i.e., the burst is sufficiently long. Hypothesis i) is generally verified, as the frequency span achievable with the IBSP is constrained by the limits of the ISM-band only. Hypothesis ii) is also typically correct since IoT radio front-ends enable adjustable central frequencies with a minimum step of 1 MHz [37]. Unfortunately, not much can be said about the veracity of hypothesis iii), as it depends on how fast is the IBSP sampling rate F_s compared to the duration of incoming bursts T_B. If it is $F_s \cdot T_B \ll 2k+1$ (see Section IV), the estimator in (11) is generally biased.

The remainder of this section focuses on low-variance estimation, deriving useful properties. Finally, we propose an estimator that, even being theoretically biased, ensures variance close to the CRLB and low bias even with incomplete sampling.

Proposition 2: If the spectrum $X(f)$ *is symmetric around* f_c, *then the variance of the estimator* $\hat{f}_c$ *in* (11) *is approximated at the* 5 % *significance level by*

$$\mathrm{Var}[\hat{f}_c] \approx \frac{N\sigma_o^2}{\mu_S^4}\left[\mu_E^2 + \mu_S^2\delta_f^2(2N^2+3N+1)/6\right], \tag{13}$$

with μ_S, μ_E, *and the c.v. constraints as in Proposition 1.*

Proof: See Appendix E. □

Theorem 2: Given the SM model and $g(n,m)$ *the value at* $f = f_0 + n\delta_f$ *of the PSD centered at* $f_c = f_0 + m\delta_f$ *of the signal to be measured, then, the CRLB of any unbiased estimator of* f_c *is*

$$\mathrm{Var}[\hat{f}_c] \geq \sigma_o^2\delta_f^2 / \sum_{n=0}^{N-1}\left(\frac{\partial g(n,m)}{\partial m}\right)^2, \tag{14}$$

where $g(n,m) \triangleq X(f_0 + n\delta_f, f_0 + m\delta_f)$ *expresses the dependence of the PSD on both the absolute frequency* $f_0 + n\delta_f$ *and its central frequency* $f_0 + m\delta_f$.

Proof: See Appendix F. □

Inequality (14) shows that the lower bound on estimation variance depends on the spectral shape of the signal to be estimated by way of its first derivative w.r.t the central frequency index m. Next, we derive more treatable bounds by making assumptions on the spectral shape of the incoming signals. The CRLBs are then experimentally verified in Section VI.

TABLE 2. Candidate central frequency estimators and theoretical characteristics.

Estimator	Method	Bias	Variance
Det	Raw detection frequency	Very Low	Uncontrolled
Max	$\arg\max_f\{Y(f)\}$	Medium	σ_o^2
E1	Implements (11)	Medium/Low	Low (13)
E2	Pre-processed E1	Very low	Low (13)

Corollary 2: If the spectrum $g(n,m)$ is triangle-shaped, hence the absolute value of its first derivative w.r.t. m calculated in its non-null region $[N_{g^-}, N_{g^+}]$ is k_s, then the CRLB for the central frequency estimator is

$$\mathrm{Var}[\hat{f}_c] \geq \frac{\delta_f^2 \sigma_o^2}{k_s^2 (N_{g^+} - N_{g^-})}, \tag{15}$$

with σ_o^2 variance of the spectrum measurement noise and $0 \leq N_{g^-} < N_{g^+} \leq N-1$.

Proof: See Appendix F. □

Corollary 3: If the spectrum $g(n,m)$ is Gaussian with parameters $\mu_g = m\delta_f$ and σ_g^2, then the CRLB for the central frequency estimator is

$$\mathrm{Var}[\hat{f}_c] \geq \frac{2\pi \sigma_g^6 \sigma_o^2 \delta_f^2}{\sum_{i=-m}^{N-m-1} i^2 \exp\left(-(i/\sigma_g)^2\right)}, \tag{16}$$

with $i \triangleq n - m$.

Proof: See Appendix F. □

Inequalities (15) and (16) provide useful lower bounds on variance, which hold in case of linear and Gaussian spectra respectively. The bounds provide baseline reference points for comparing the performance of candidate estimators when the format of the spectra to be measured are unknown, or its closed-form expression is unavailable.

D. THE PROPOSED ESTIMATORS

Based on the mathematical insights of Section V-C we define four estimators of increasing complexity. We introduce their setup and highlight the salient properties in Table 2.

- $\hat{f}_c^{(\mathrm{Det})}$ is the most straightforward estimator, where the estimated spectral center is the detection frequency of the interference burst. It requires virtually no processing time, and it is expected to provide unbiased estimation for signals with symmetrical PSD. Unfortunately, its variance is governed by the variance of the detection frequency; hence, it is expected to grow unacceptably for wide-band signals.

- $\hat{f}_c^{(\mathrm{Max})}$ estimates f_c with $\arg\max_f\{Y(f)\}$, therefore the maximum-amplitude sample locates the central frequency. It is a suitable choice when the entire IBSP is explored and the samples have a low-noise level. It requires a maximum search within a sample set with a cardinality of at most $2k+1$. Two important drawbacks are that i) the estimation variance is directly linked to the measurement noise variance, and ii) its bias is strongly affected by missing samples.

- $\hat{f}_c^{(\mathrm{E1})}$ is a direct implementation of (11). The estimator has theoretical low bias (12) and low variance (13) with large sample sets. Nevertheless, both the bias and the variance are expected to worsen in real cases due to incomplete IBSP sampling, which reduces the SNR μ_S^2/σ_o^2 and causes asymmetry around f_c.

- $\hat{f}_c^{(\mathrm{E2})}$ requires three additional steps after calculating $\hat{f}_c^{(\mathrm{E1})}$. First, the sample set is pre-processed, and a LI version of the observed spectrum is generated. Second, (11) is re-evaluated over the LI spectrum and centering the estimation on $\hat{f}_c^{(\mathrm{E1})}$. Finally, the theoretical bias is calculated with (12) and corrected. These steps aim to improve the performance in the presence of short bursts (i.e., few samples), while its gain over $\hat{f}_c^{(\mathrm{E1})}$ is expected to be negligible for long bursts.

TABLE 3. Specifications of the test signals.

Label	Modulation Scheme	I/Q Sample Rate	BB Filter	Total BW
A	BPSK	8 MS/s	RC	6.6 MHz
B	O-QPSK	33 MS/s	RRC	15.8 MHz
C	OFDM (QAM)	10 MS/s	-	4.1 MHz
D	None (WGN)	[5, 25]MS/s	-	variable

VI. EXPERIMENTAL ANALYSIS

This section analyzes the performance of spectrum estimation in a controlled measurement setting. Later, Section VII complements the analysis with a use-case in a CR link.

A. EXPERIMENTAL SETUP

The proposed method, including all the modules of Fig. 2, is implemented in Contiki OS and entirely executed on the IEEE 802.15.4 compliant Crossbow TelosB platform [46], based on the TI-CC2420 transceiver [39]. Since the platform poses several hardware constraints, both on the radio and processing capabilities, it is an excellent candidate for testing the proposed method. The implementation-specific parameters are given in Table 1. A complete (51, 25)-IBSP, optimized as described in Section IV, is implemented in the platform, providing analysis of radio bursts with up to 51 MHz bandwidth. The reference signals are generated via the software-defined radio (SDR) NI-USRP 2921. The signals, listed in Table 3, have different modulation schemes, I/Q rate, and baseband (BB) filters, which provide diverse spectral footprints. A third device, the USRP N210, which is used for validation purposes, samples the generated signals with a sample rate of 50 MS/s, and computes the reference spectra via FFT. In Table 3, we show the total bandwidth of the reference signals measured with an SNR of approximately 80 dB. In order to eliminate the effects of radio-channel and external RF noise, we use a direct RF port-to-port connection via RF pigtails for both the SDR and the TelosB device.

B. CENTRAL FREQUENCY ESTIMATION

The first series of experiments analyze the accuracy of the central estimators proposed in Section V-C. The estimation system is tested with signal D with 45 MHz bandwidth and variable burst duration ranging from 0.4 ms to 8 ms. Particularly, 0.4 ms meets the physical limit of our TelosB implementation (i.e., only three samples are collected), due to the maximum achievable sampling rate of IBSPs reported

TABLE 4. Bandwidth estimation error (MHz) of spectrum reconstructed with linear interpolation (LI) and spectrum Models (RC, HT, GS, and MM). In bold the lowest mean estimation error.

Signal Label	BW Definition	Reference Value	Model LI	RC	HT	GS	MM
A	6 dB (σ)	0.4 MHz	−0.6 (0.2)	−3.4 (4.2)	−2.0 (2.0)	**−0.6 (0.2)**	−1.2 (1.2)
	ENB (σ)	0.2 MHz	−1.3 (0.3)	−4.5 (4.0)	−2.3 (2.0)	**−0.9 (0.4)**	−1.5 (1.3)
	Total (σ)	0.7 MHz	−1.2 (0.4)	−5.4 (5.6)	−2.3 (3.6)	**−0.4 (0.6)**	−1.0 (1.4)
B	6 dB (σ)	6.3 MHz	3.1 (1.7)	−2.0 (3.4)	−6.7 (3.4)	0.8 (6.5)	**−0.2 (3.5)**
	ENB (σ)	2.1 MHz	3.9 (1.8)	−3.2 (4.5)	−4.3 (6.0)	2.9 (1.3)	**1.3 (4.2)**
	Total (σ)	10.5 MHz	2.1 (2.3)	2.4 (3.5)	−5.0 (5.8)	**1.7 (1.6)**	3.6 (4.7)
C	6 dB (σ)	2.3 MHz	−3.4 (3.1)	−4.6 (4.4)	−3.5 (4.0)	**−0.9 (2.6)**	−2.3 (3.7)
	ENB (σ)	1.2 MHz	−3.0 (2.7)	−4.4 (4.8)	−2.6 (4.0)	**−0.5 (3.2)**	−1.9 (4.1)
	Total (σ)	3.1 MHz	−1.7 (1.7)	−3.6 (4.4)	−2.4 (4.1)	0.3 (2.6)	**0.3 (1.0)**

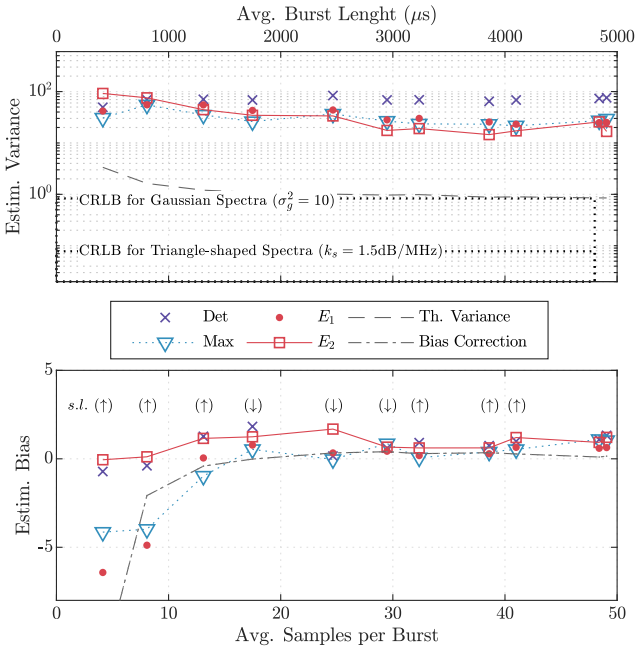

FIGURE 4. Experimental validation of the candidate f_c-estimators, with theoretical CRLBs (15), (16), bias correction (12) with 5 % significance level (*s.l.*) test (↑↓), and theoretical variance (13).

in Table 1. Fig. 4 reports the estimation accuracy expressed in terms of the estimation bias and variance, showing a good fit with the theoretical properties in Table 2. Notably, using the detection frequency as an estimator (i.e., $\hat{f}_c^{(\mathrm{Det})}$) ensures low bias but shows no variance reduction from using more samples, which reflects into mediocre performance. The estimator $\hat{f}_c^{(\mathrm{Max})}$ provides instead a more reasonable compromise between simplicity and performance, showing a standard deviation between $6-8$MHz. Unfortunately, $\hat{f}_c^{(\mathrm{Max})}$ shows considerable bias when operating with less than 10 samples, which renders it unsuitable for profiling sub-ms radio-bursts. The implementation of (11) alone does not seem to be particularly promising as $\hat{f}_c^{(\mathrm{E1})}$ shows similar bias and variance performance w.r.t. $\hat{f}_c^{(\mathrm{Max})}$ but requires the computation of the terms E and S of (11). Finally, $\hat{f}_c^{(\mathrm{E2})}$ provides the best performance in terms of bias, which is always lower than 1.6 MHz for any recorded burst-duration while its variance matches $\hat{f}_c^{(\mathrm{Max})}$. A substantial benefit of $\hat{f}_c^{(\mathrm{E2})}$ comes from the bias correction term, calculated in real-time with direct implementation of (12). Fig. 4 shows the important effect of this term for sub-ms radio-bursts, together with the 5 % significance level test of Proposition 1.

1) VARIANCE BOUNDS

In Fig. 4 we show the CRLBs derived in (15), and (16) where the parameters k_s and σ_g^2 of the Gaussian and triangle-shaped spectral models are determined by fitting the models to the reference spectrum. In particular, the triangle-shaped spectrum shows lower CRLB than the Gaussian spectrum, which is due to the smoothness of the Gaussian spectrum, leading to a low-valued first derivative $\partial g(n,m)/\partial m$. As expected, the higher the variation of the spectrum $g(n,m)$ with respect to the central frequency bin m, the lower is the attainable estimation variance. On the other hand, approaching the CRLB seems unrealistic for LC-IoT hardware, since the non-negligible RBW smoothens the measured spectrum, as discussed in Section IV. For this reason, the use of platforms ensuring narrow/tunable channel filter, hence lower RBW, is preferable, as the impact on estimation variance can be contained. We believe that a more relevant bound can be obtained by repeating the proofs of (16) and (15), and substituting $g(n,m)$ with its frequency-domain convolution with the frequency response of the employed channel filter. Unfortunately, such quantity does not generally have a closed-form expression, unless a model of the real filter response is taken. Finally, we highlight the role of the frequency granularity, as the CRLB grows quadratically with δ_f in (14). While in the tested platform, δ_f is 1 MHz, the capability to select frequency on a smaller scale is expected to lower the achievable CRLB and improve the estimation variance (13).

C. SPECTRAL ESTIMATION

We employ the signals A, B, and C in Table 3 to test the accuracy of spectrum estimation. Specifically, we record the output of the different spectrum models and the linear interpolation (LI) and evaluate their goodness-of-fit w.r.t. the reference spectra. In this experiment, we target the assessment of the model-fitting process only, by ensuring a fixed number of samples in the $(51, 25)$-IBSP measurement process. The effect of incomplete sampling is then separately studied in Sections VI-B and VI-D. Table 4 summarizes the estimation error for different bandwidth definitions, i.e., 6 dB-bandwidth, equivalent noise

TABLE 5. Distortion of reconstructed spectrum and % of model selection in MM (lowest MSE). In bold, the lowest distortion.

Signal Label	Metric	Model LI	RC	HT	GS	MM
A	% LSE	-	4 %	23 %	73 %	-
	LSD (dB)	7.6	12.5	7.6	8.1	**7.4**
	PSNR (dB)	**−0.6**	−5.0	−1.0	−1.3	−0.8
B	% LSE	-	57 %	5 %	38 %	-
	LSD (dB)	15.8	11.7	13.6	**8.4**	10.6
	PSNR (dB)	−6.8	−4.4	−5.7	**−0.1**	−3.0
C	% LSE	-	0 %	0 %	100 %	-
	LSD (dB)	5.9	6.9	5.7	**5.5**	5.7
	PSNR (dB)	−0.3	−1.1	0.1	−0.1	**0.2**

bandwidth (ENB), and total bandwidth, calculated as an equivalent 20 dB-bandwidth. The estimation error is calculated as the difference between reference and estimated bandwidth so that a negative value indicates bandwidth overestimation. The multi-model (MM), i.e., the lowest-MSE model for each burst, and the Gaussian Spectrum (GS) model ensure the most stable performance over the different signals, with the GS model fairing better than the MM with signal A. We observe that, despite its simplicity, the LI model shows acceptable bandwidth estimation performance for signals which are narrowband w.r.t. the RBW of the detection system. Conversely, LI performs considerably worse than the MM and GS models for larger bandwidths (i.e., signal B), as it fails to compensate for the incomplete IBSP-sampling. The RC and HT models tend to overestimate the bandwidth of all the reference spectra.

Table 5 analyzes the goodness of spectral reconstruction by means of the log-spectral distortion (LSD) measure, which is defined as $D_L^2 = \sum_{i=0}^{N-1}[10\log_{10}(\hat{Y}(f_0 + i\delta_f)/Y(f_0 + i\delta_f))]^2$, with $Y(f)$ and $\hat{Y}(f)$ reference and estimated PSD over N-spectral points, and δ_f as defined in Table 1. The peak signal-to-noise ratio (PSNR) is given as a support metric. Similarly to the bandwidth estimation test, we observe that the MM and GS models ensure the best performance for all the tested signals. As expected, the LI method provides adequate spectral fitting with narrowband signals but suffers 5 dB-higher LSD than the MM with signal B. Table 5 also shows the probability of the candidate models being selected in the MM, i.e., producing the MMSE solution. The results show that the GS model is chosen frequently with signals A and C, while its selection rate drops with signal B. This is likely driven by the employed root-raised-cosine (RRC) pulse-shaping filter reflecting into a spectrum with steeper roll-off, which is better accommodated by the RC model. The overall results show that there is a certain advantage of using more complex models rather than simple interpolation, and the advantage grows as the bandwidth of the signal increases w.r.t. the RBW of the IoT system. Ultimately, the configuration for the spectrum reconstitution block should be dictated by the requirements of the target use-case. Particularly, if the accurate reconstruction of the spectral shape is relevant to the application (e.g., wireless-technology identification), the use of the MM is advised.

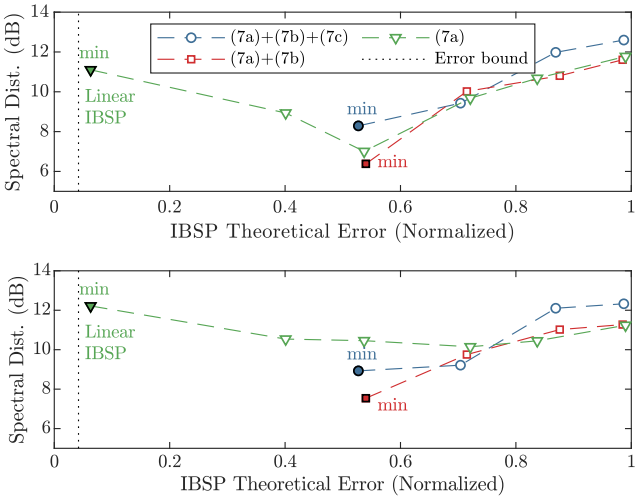

FIGURE 5. IBSP error vs. distortion of estimated spectrum; 32 samples (top) and 12 samples analysis (bottom), effect of constraints in (7), and error bound (6).

D. THE INFLUENCE OF IBSP ERROR PROPERTIES

The analysis in Section IV predicts that the selection of the IBSP influences the cumulative sampling error. This section targets the experimental validation of the assumption and ultimately evaluates the impact of the sampling error on the spectrum estimation accuracy.

Fig. 5 analyzes how the cumulative error of the IBSP influences the LSD of the reconstructed spectrum. The non-linear integer program (7) is solved for different setups of constraints, yielding sampling patterns with different error properties, which we program into the spectrum estimation module. In Fig. 5 (top), we show the LSD for signal bursts recorded with a mean number of 32-samples, meaning that around 62 % of the (51, 25)-IBSP is exploited. Three essential results arise from this case: i) there is a significant difference (6 dB) between the spectral distortion achievable with the least and the most errored IBSPs, ii) the best unconstrained-solution (i.e., the linear IBSPs) worsens the LSD of about 5 dB w.r.t the best constrained-solution, and iii) the minimum solution obtained by disengaging the frequency-correlation constraint (7d) is marginally more favorable than the one with full-constraints. Fig. 5 (bottom) shows the estimation behavior with shorter radio-bursts, which leads to exploring only 24 % of the IBSP. In this case, the linear IBSPs perform equally poorly, which strengthens the hypothesis that linear IBSPs are unsuitable in case of fast radio bursts or slow sampling. Particularly, the analysis of estimation performance of (51, 25)-IBSPs with an exploration ratio of 20 % to 25 % is important since i) the related[2] burst duration is in the order of magnitude of 1 ms, which is fairly common for IoT wireless standard, and ii) the explored spectrum is 51 MHz, which approaches

[2]With respect to the IBSP sampling rate of ≈ 10 kS/s achievable with the target LC-IoT platform.

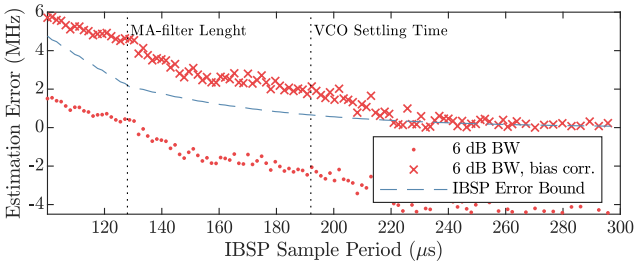

FIGURE 6. Fast vs. accurate sampling: trade-off between IBSP period and bandwidth estimation error with CC2420 radios. A rescaled version of the theoretical error bound (6) is shown as a reference.

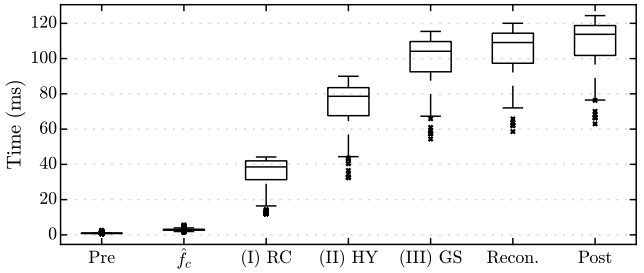

FIGURE 7. Cumulative processing time of the TI-MSP430 implementation for different steps of spectrum estimation.

the largest signal bandwidth in the 2.4 GHz ISM-band (i.e., IEEE 802.11ac/ax). Finally, we conclude that the inclusion of platform constraint (7c) in the non-linear program (7) is vital for ensuring optimal sampling performance.

We investigate the effects of different sampling periods in Fig. 6. A variable sampling delay has been implemented in the TelosB platform to progressively relax its IBSP sampling rate and reveal the impact of the different sample-rate-dependent error components (VCO stabilization, MAF), as they act on slightly different time-scales. In particular, we analyze how the bandwidth estimation is affected by different sampling periods. To isolate the effect, we ensure a constant amount of IBSP samples. In Fig. 6 we also overlay the theoretical error bound (6) to give a visual reference on the predicted error trend. The experiment proves that the estimation error is stable for sample periods longer than 210 µs, which supports the assumptions made in Section IV about the time-domain characterization of the IBSP-error, as the VCO is expected to be substantially stable after 192 µs.

E. ON PROCESSING REQUIREMENTS

The implementation of runtime spectrum estimation in LC-IoT hardware entails important design choices. The most notable trade-off is the unfeasibility of floating-point arithmetic and the need to use heavily-optimized custom implementations of mathematical functions. For ensuring realistic processing time on the employed platform (which relies on a TI-MSP430 microcontroller), we rely on look-up tables and second-order Taylor approximations for exponential and trigonometric functions in the models. Fig. 7 shows the cumulative distribution of processing time for the full-model spectrum reconstruction, divided by processing steps. The most burdensome step is the multi-model fitting, which takes on average 89 % of the total time. The LI method (included in the pre-processing stage) provides indeed a much faster - yet less accurate - alternative, which executes in 5.7 ms on average, including central frequency estimation. These results are strongly platform-dependent, which is good news as newer IoT platforms systematically outperform the MSP430. Lastly, ensuring fast processing is crucial to bound the sensing and estimation period in spectrum sensing strategies, as we show in Section VII.

F. REMARKS

A high IBSP sampling rate has two contrasting effects. On the one hand, it allows profiling shorter (hundreds of µs) radio bursts, which are common in IoT-related RF transmissions. On the other hand, it worsens the estimation performance as it collides with the slow dynamics of onboard VCO-tuning and RSSI-computation. Employing optimized IBSPs greatly enhances the estimation process allowing spectrum estimation of bursts with durations down to 400 µs even with fairly old radio platforms. Thanks to optimized IBSPs, real-time spectral reconstruction can be achieved even with LI methods only, leading to 5 ms to 6 ms execution time, when a trade-off with estimation accuracy is possible. When the platform allows it, a complete multi-model LSE approach is beneficial for improving the accuracy of the estimated spectrum.

VII. USE CASE—ANTICIPATIVE BLACKLISTING WITH SPECTRAL ESTIMATION

Lightweight and onboard spectrum analysis provides compelling opportunities for cognitive and dynamic medium access, even when the network is exclusively composed of LC-IoT devices. Although a thorough exploration of such applications is outside the scope of this work, we present a relevant use-case where the proposed method reinforces an industrial IoT standard with real-time Spectrum Estimation and Anticipative Blacklisting (SEAB).

A. THE SEAB APPROACH

We developed SEAB to safeguard the performance of ISA100.11a [11] wireless industrial standard in the presence of severe interference by augmenting its TSCH mechanism. In SEAB, the receiver node proactively scans the ISM-band in between two consecutive data-transmissions and analyzes at runtime the spectrum of detected radio bursts to identify repeating high-energy bursts. The receiver exploits the spectrum data to update a 1 MHz-resolution spectral map, which is, in turn, used to update a dynamic channel blacklist. The state of the blacklist reflects the spectrum shape of the newly detected bursts and information about the previous state of the spectrum. The blacklist is then uploaded to the transmitter using three short feedback packets, shielded using redundancy and frequency diversity, and immediately used

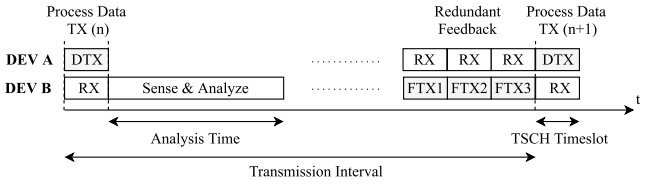

FIGURE 8. Time-diagram of the SEAB coordination mechanism.

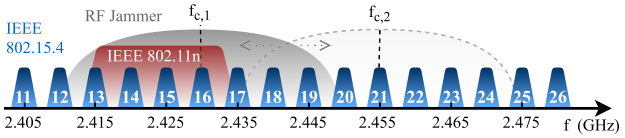

FIGURE 9. Spectral allocation of the radio-systems in the experiments.

to adapt the channel-hopping sequence in the next scheduled transmission. The coordination scheme loosely resembles the sensing and report sections for the IEEE 802.15.4 slot-frame that Chiti et al. propose in [47], which is only based on threshold-based detection of PUs. Later, as the interfering signal ceases, the channels are progressively re-allocated and can be used again for data transmission. The employed mechanism and the associated timings are reported in Fig. 8.

B. EXPERIMENTAL SETUP

1) RADIO-LINK

We establish an indoor 10 m-LoS radio-link between two TelosB nodes. The devices are programmed with a TSCH scheme following[3] the ISA100.11a Index 1 specifications [11]. The transmission of IEEE 802.15.4 maximum-size packets is uni-directional and periodic (2 s), representing a rather general use case in slow-periodic open-loop wireless-control schemes [48]. The SEAB spectrum management system, built on an optimized version of the spectrum estimation solution, operates on top of the TSCH mechanism. Given the hardware limitations of the platform, few adjustments are necessary to ensure compatibility with the employed communication scheme. In particular, only the GS model is used, and the number of bursts analyzed per scanning session is constrained to minimize the spectrum analysis time, which is sketched in Fig. 8.

2) INTERFERENCE

The radio link is exposed to two types of RF disturbances: time-varying broadband RF jamming, and IoT cross-technology interference. The jammer is a USRP device [49] emitting signal D (see Section VI-A) with approximately 40 MHz of total bandwidth, 10 ms bursts with 50% duty cycle, at the maximum power allowed by the hardware. The center frequencies 2.43 GHz and 2.455 GHz are alternated on a 180 s-basis. The signal falls in the domain of partial-band time-varying jamming [7]. In the second experiment, the jammer is replaced with an IEEE 802.11n access point in 20 MHz-mode generating a continuous data-stream on IEEE 802.11 channel 3, while the same layout of the jamming experiment is retained for a fair comparison. An overview of the described spectral allocation is given in Fig. 9.

C. REAL-TIME QoS METRICS

The main advantage of SEAB compared to a posteriori spectrum management is the fast reaction time, i.e., the channel is blacklisted before its communication quality is affected. For this reason, we drop long-term-averaged performance metrics and favor a QoS analysis centered on real-time indicators and worst-cases. We adopt: 1) the (n, k)-firm deadline for streams with real-time requirements introduced by Ramanathan et al. in [50], which is satisfied if at least n over the last k packets are correctly decoded, and 2) the number of consecutive dropped/missed packets. The selected metrics are especially relevant for industrial control [51] and cyber-physical systems, where the resilience to external disturbances plays a vital role in ensuring that deadlines for the real-time tasks are met [52].

D. RESULTS AND ANALYSIS

1) STEADY-STATE ANALYSIS

First, we use the (n, k)-firm deadlines metric to assess the probability of dynamic failure [50], i.e., the probability of the ISA100.11.a communication violating the (n, k)-firm deadlines on packet delivery for some $x = n/k$. In Fig. 10, we show the analysis over 1122 packets (37 min), repeated for two different arbitrary values of k, when the TSCH link is affected by the described time-varying RF jamming signal. The figure shows that the jamming signal is deadly for the radio-link even when adopting the TSCH diversity scheme, inflicting a dynamic failure probability of 0.82 for (4, 5)-firm deadlines and greater than 0.9 for (24, 30)-firm deadlines (point $x = 0.8$ in Fig. 10). The result suggests an important benefit of SEAB over pure TSCH, with the CDF curves considerably shifting towards the interference-free case and with the dynamic failure probability reduced to 0.38 and 0.03 for the (4, 5) and (24, 30)-firm deadlines respectively. SEAB ensures $(n, 5)$-firm deadline close to no-interference case for $0 \leq n \leq 3$, since at least 3 out of the last 5 packets are correctly received 95.4 % of the time, with 99.8 % for the interference-free scenario. This leads to a considerable reduction of the cumulative (3, 5)-dynamic failure time, i.e., the aggregated time where less than 4 out of the last 5 packets are received, from 346 s to 24 s.

In Fig. 10, we also show the behavior of static-channel communication as a reference, with the selected channel lying within the band affected by the jammer. Unacceptable real-time performance is reported with the CDF of dynamic failures always above 0.4 due to long strikes of missed packets, as the time-frequency overlap of interference and signal bursts frequently brings the IEEE 802.15.4 PHY below its optimal SNR region. The analysis is repeated when the SDR is substituted with an IEEE 802.11n access point, maintaining the same experimental layout. In this case, the performance drop is less severe, yet the SEAB spectrum management

[3]Due to the hardware constraints of TelosB motes, the duration of time slots is 20 ms in place of the ISA100.11a-compliant 10 ms or 12 ms

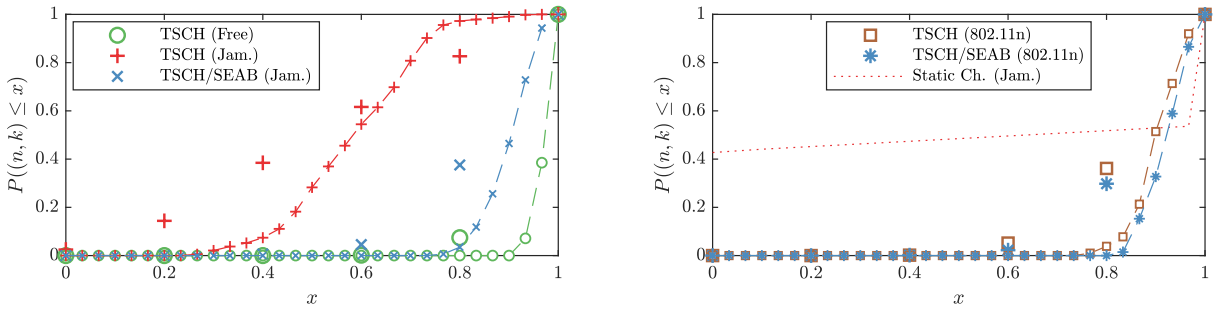

FIGURE 10. Empirical CDF of dynamic failures for different (n, k)-firm deadlines (x) in case of $k = 5$ (big markers) and $k = 30$ (dotted line/small markers).

TABLE 6. Real-time QoS analysis: Mean (μ) and worst case ($w.c.$) of $(n, 5)$-ratio on packet delivery, consecutive transmission failures (CTF) and communication blackout duration (CBD).

Method	Metric	Interference Source: None		802.11n		RF Jammer	
		μ	$w.c.$	μ	$w.c.$	μ	$w.c.$
TSCH	$(n, 5)$	4.92/5	4/5	4.59/5	2/5	3.01/5	0/5
	CTF	1.000	1	1.042	2	1.928	7
	CBD	2 s	2 s	2.08 s	4 s	3.86 s	14 s
TSCH with SEAB	$(n, 5)$	4.92/5	4/5	4.68/5	2/5	4.57/5	2/5
	CTF	1.000	1	1.032	2	1.062	2
	CBD	2 s	2 s	2.06 s	4 s	2.12 s	4 s

leads to a 7 % reduction of dynamic failures of $(3, 5)$-firm deadlines. This can be interpreted as a positive side-effect of SEAB, as the solution is programmed to intervene only in the presence of wide-band, high-power, and high duty-cycle interference. Since the 20 MHz-wide IEEE 802.11n signal format resembles some of the characteristics of the jamming signals, SEAB autonomously blacklists a subset of the overlapped channels, leading to the observed performance increase. Finally, Table 6 sums up the analysis showing the mean and worst-case performance of the ISA100.11 link in the described scenarios. In the table, we also report the number of consecutive transmission failures, which we analyzed later in this section, and the duration of communication blackouts, i.e., a period with no successful transmission.

2) TRANSIENT-STATE ANALYSIS

The key-features of SEAB are the burst-based spectrum estimation and the channel adaptation process executed before each transmission. This means that the hopping sequence is promptly adapted based on the newest available channel states. In Fig. 11, we show how this reflects into a fast blacklisting in case of sudden and severe interference. The beneficial result is that the QoS undergoes virtually no transient-state with performance deterioration before being addressed. While it takes on average 9.9 s to have at least 90 % of the affected channels blacklisted, in 93 % of the experiments at least one channel was blacklisted before the first data-transmission in the presence of jamming. This means that while SEAB requires a certain time to bring the channel-list to a steady-state, the most affected channels undergo immediate (first estimation cycle) blacklisting, which helps to safeguard the QoS. The channel list is then gradually restored to its original state (de-blacklisting)

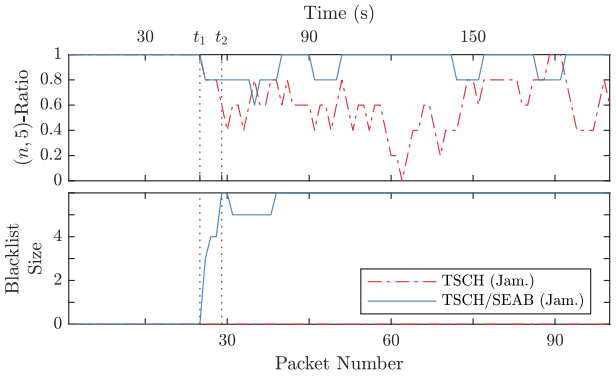

FIGURE 11. Transient-state behaviour: evolution of $(n, 5)$-ratio and blacklist since jammer activation (t_1) and 90 % of final blacklist size (t_2).

when the cause, i.e., the jammer, is removed. The described dynamic, visible in Fig. 11, helps explaining the significant improvement over the pure ISA100.11a TSCH scheme reported in both Table 6 and Fig. 10. The proposed mechanism also is helpful in minimizing the occurrences of consecutive transmission failures, as it is shown in Fig. 12. The ISA 100.11a hopping sequences are indeed designed to limit the number of consecutive failures induced by IEEE 802.11 WLANs, which explains why they perform quite poorly when exposed to strong wide-band interference with dynamic spectral features. Fig. 12 shows how the adaptivity of SEAB outclasses the original TSCH scheme in the presence of jamming by manifesting strikes of two consecutive transmission failures in only six occurrences over 1122 packets.

3) CHANNEL PERFORMANCE

Lastly, we show in Fig. 13 long-term channel-specific statistics on the packet delivery ratio (PDR) in the different experiments. From the figure, the reader can infer the set of channels more affected by the jammer, and how SEAB helps to dynamically rearrange the TSCH sequence over the best performing channels, according to the current spectrum state. As a result, the PDR of the basic TSCH scheme is improved on all the available channels. In particular, we observe that some channels (e.g., 20 to 23) show a dramatic PDR boost, as SEAB well-adapts to the slow frequency-switching nature

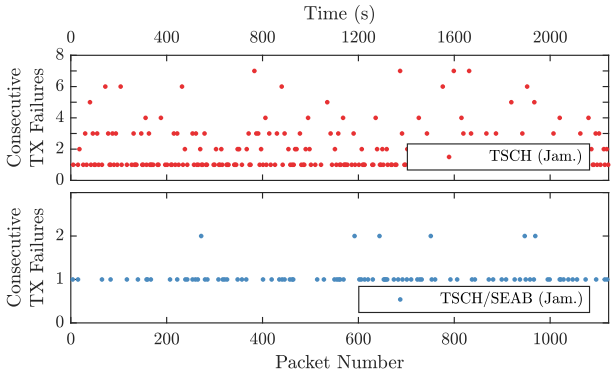

FIGURE 12. The effect of SEAB in the mitigation of consecutive transmission failures.

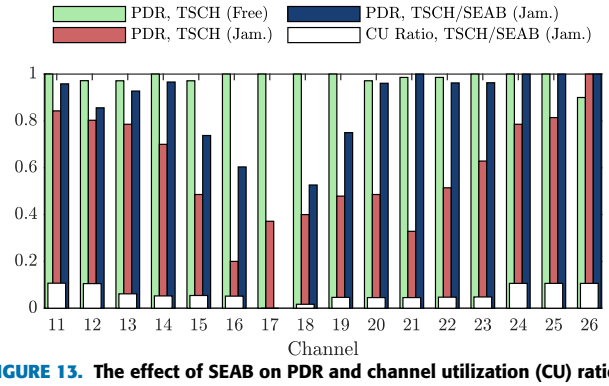

FIGURE 13. The effect of SEAB on PDR and channel utilization (CU) ratio.

of the jammer avoiding over-blacklisting. Only in one case (channel 17), the channel is never allowed in the TSCH pattern, as SEAB constantly detects a spectral tail of the jamming signal.

E. REMARKS

The examined use-case is a limited but promising proof-of-concept of reliable wireless communication with soft real-time requirements for devices with modest hardware capabilities in unpredictable RF scenarios. On the other hand, we recognize that there are many other potential applications for the proposed spectrum estimation method. Moreover, there is a long road ahead to turning spectrum estimation with LC-IoT hardware into reliable communication, with the grand-challenge represented by applications with real-time requirements. We, therefore, leave future works to exploit the potential of lightweight spectrum analysis in the context of dynamic spectrum allocation, unsupervised classification of IoT technologies, detection, and avoidance of RF jammers of different natures (e.g., fast-sweeping jammers [7]).

VIII. CONCLUSION

There is an evident gap between state-of-the-art spectrum analysis techniques and the actual implementations hitting the IoT market. Besides, the work of the cognitive radio research community shows a division between the spectrum sensing methods, which focus on primary user detection, and sophisticated signal analysis relying on high-resolution measurements, which are unsuitable for low-complexity IoT (LC-IoT) hardware. This work strives to bridge the two approaches by proposing a spectrum analysis method that substantially differs from the proposals in the literature, and ensures suitability for a large family of LC-IoT devices. The method proves that signal burst detection, intra-burst swept sampling, and ultimately parametric spectrum reconstruction, are possible even on severely-constrained devices. The solution produces a spectrum estimate of single signal bursts requiring a sampling rate of two to three orders of magnitude below the Nyquist rate. As the method borders the capabilities of LC-IoT radios, ad hoc sampling patterns with optimal error properties are demanded. We have presented the mathematical setting of such an optimization problem for radio platforms with different characteristics and experimentally validated the method by showing the tangible impact of optimal patterns on the accuracy of the reconstructed spectrum. Tests in a controlled RF environment have shown the advantage of employing parametric spectrum models, as well as the baseline performance of lightweight interpolation, which is a viable spectrum reconstruction alternative for extremely constrained platforms. Finally, we have proven the tangible benefit of the proposed spectrum estimation solution by augmenting a TSCH link under substantial RF interference. We have verified that the proposed method identifies and adapts to the spectral footprint of the interfering signals in a proactive manner providing over 50 % improvement of real-time PDR and a 71 % reduction of the worst-case outage time.

APPENDIXES

APPENDIX A
PROOF OF LEMMA 1

Any (l, k)-IBSP can be constructed by choosing from a set of $2k + 1$ distinct elements, hence there are $(2k + 1)^l$ distinct IBSPs. If the IBSP is complete, each element has to be unique since Definition 2. It follows that the total number of $(2k + 1)$-complete IBSPs is $\prod_{i=1}^{2k+1} i = (2k + 1)!$.

APPENDIX B
PROOF OF THEOREM 1

It is needed to minimize $\mathcal{E}_{lin}$ in (5) w.r.t. the IBSP S. We examine the first two terms $E_{C,lin}$ and $E_{V,lin}$ separately as they depend on S. The study of $E_{C,lin}(S) = k_f \delta_f \sum_{i=1}^{l-1} \sum_{j=i}^{L_c} C(jT_s)\,|s_i - s_{i-j}|$ reveals that the dependence from the IBSP S manifests through the difference $|s_i - s_{i-j}|$. With $L_c = 1$, it is $E_{C,lin}(S) = k_f \delta_f C(T_s) \sum_{i=1}^{l-1} |s_i - s_{i-1}|$. From Definition 2 follows that, if $s_i, s_j \in S$, and S is (l, k)-complete it is $s_i \neq s_j$, $\forall i \neq j$. Thus, the problem of minimizing $E_{C,lin}$ is equivalent to the problem of arranging l-unique integers (with $l = 2k + 1$) $s_0, \ldots, s_{l-1}$ in the interval $[(-l + 1)/2, (l - 1)/2]$ such that the sum $\sum_{i=1}^{l-1} s_i$ is minimized. The problem has trivial solution since the minimum distance between two elements of any complete IBSP is unitary and only two minimum-sum configurations exist,

which are $S_m = \{(-l+1)/2, (-l+3)/2, \ldots, (l-1)/2\}$ and its reverse $S'_m = \{(l-1)/2, (l-3)/2, \ldots, (-l+1)/2\}$. Then, it is $E_{C,lin}(S_m) = E_{C,lin}(S'_m) = (l-1)\, k_f \delta_f C(T_s)$.

The analysis of the VCO-related error term $E_{V,lin}(S) = k_f \delta_f^2\ g_V(T_s) \sum_{i=1}^{l-1} |s_i - s_{i-1}|^2$ follows the same reasoning, since $\min\{|s_i - s_{i-1}|^2\} = 1$, then both S_m and S'_m minimize the error component so that $E_{V,lin}(S_m) = E_{V,lin}(S'_m) = k_f \delta_f^2 (l-1)\delta_f g_V(T_s)$. Since the additive noise term $n(i)$ does not depend on S, the cumulative error becomes

$$\mathcal{E}_{lin}(S) \ = \sum_{i=0}^{l-1} n(i) + (l-1)\, k_f \delta_f \big[C(T_s) + \delta_f g_V(T_s)\big]. \quad (17)$$

Since $n(i)$ is an AWGN term, $\mathcal{E}_{lin}(S)$ follows a Gaussian distribution with mean $(l-1)\, k_f \delta_f \big[C(T_s) + \delta_f g_V(T_s)\big]$ and variance $l\, \sigma_N^2$. Therefore, if the statistical expectation operator is applied to both members and it is noted that both the terms $E_{C,lin}$ and $E_{V,lin}$ are minimized by S_m and S'_m, the lower bound of (17) follows as $\mathbf{E}\,[\mathcal{E}_{lin}(S)\,] \geq (l-1)\, k_f \delta_f \big(C(T_s) + \delta_f g_V(T_s)\big)$, which is true for any complete (l, k)-IBSP S, thus verifies the thesis in (6).

APPENDIX C
PROOF OF COROLLARY 1

The IBSPs S_{lin} and S'_{lin} are complete since Definition 2. The optimality of both IBSPs simply follows from the proof of Theorem 1, since (17) is true only for $S = S_{lin}$ or $S = S'_{lin}$.

APPENDIX D
PROOF OF PROPOSITION 1

The expected value of $\hat{f}_c$ is derived from (11) as $\mathbf{E}[\hat{f}_c] = f_0 + \mathbf{E}\left[\sum_{n=0}^{N-1} n\delta_f Y[n] / \sum_{n=0}^{N-1} Y[n]\right]$. Given the SM model, the argument of the expected value is a ratio of two Gaussian random variables E and S, with distribution $\mathcal{N}(\mu_E, \sigma_o^2 \delta_f^2 \sum_{n=0}^{N-1} n^2)$, and $\mathcal{N}(\mu_S, N\sigma_o^2)$, respectively, with $\mu_S \triangleq \sum_{n=0}^{N-1} X[n]$ and $\mu_E \triangleq \sum_{n=0}^{N-1} n\delta_f X[n]$. The ratio distribution W is a Cauchy-Lorentz [53] which has undefined statistical moments, hence undefined bias. Therefore, we use the result of [54] to approximate the ratio $W = E/S$ as normally distributed at the 5 % significance level if the coefficients of variation are $c.v.(S) \geq 0.005$, and $c.v.(E) \leq 0.39$. If W is normally distributed, then the second-order Taylor series also approximates the first two moments of W with 5 % significance level, so that $\mathbf{E}[W] \approx \mu_E/\mu_S + \sigma_S^2 \mu_E/\mu_S^3 = \sum_{n=0}^{N-1} n\delta_f X[n] / \sum_{n=0}^{N-1} X[n] + \sigma_o^2 N \mu_E/\mu_S^3$, as shown in [54]. Then, it is $\mathbf{E}[\hat{f}_c] \approx (f_0 + \mu_E/\mu_S) + \sigma_S^2 \mu_E/\mu_S^3$. Recognizing that first term of the sum gives the central frequency of symmetric spectrum $X(f)$ centered in $f_c = f_0 + m\delta_f$, with $0 \leq m \leq N-1$, leads to the approximation $\mathbf{E}[\hat{f}_c] \approx f_c + \sigma_o^2 N \mu_E/\mu_S^3$ which is true with 5 % significance level, proving the thesis in (12).

APPENDIX E
PROOF OF PROPOSITION 2

Analogously to Proposition 1, the estimation variance $\mathrm{Var}[\hat{f}_c] = \mathrm{Var}[f_0 + E/S]$ can be approximated with the second-order Taylor expansion [54] so that $\mathrm{Var}[\hat{f}_c] \approx \sigma_S^2 \mu_E^2/\mu_S^4 + \sigma_E^2/\mu_S^2$ with 5 % significance level if $c.v.(S) \geq 0.005$ and $c.v.(E) \leq 0.39$. Then, we express $\sigma_E^2 = \mathrm{Var}[\delta_f \sum_{n=0}^{N-1} nN_o[n]] = \delta_f^2 \sigma_o^2 (2N^3 + 3N^2 + N)/6$ where the Faulhaber's formula [55] gives the closed-form of the sum. Also, it is $\sigma_S^2 = \mathrm{Var}[\sum_{n=0}^{N-1} N_o[n]] = N\sigma_o^2$. Plugging σ_E^2 and σ_S^2 in the expression of $\mathrm{Var}[\hat{f}_c]$ and rearranging the terms in N proves the thesis.

APPENDIX F
PROOF OF THEOREM 2

Let $\mathbf{Y} = \mathbf{X} + \mathbf{N_o}$ be the AWGN measurement of the SM model. The spectrum to be estimated can be written as a function of both its central frequency $f_c = f_0 + m\delta_f$ and the absolute frequency $f = f_0 + n\delta_f$ as $g(n, m) \triangleq X(f_0 + n\delta_f, f_0 + m\delta_f)$. Its log-likelihood function [56] is

$$\ln p(\mathbf{Y}, m) = -\frac{N}{2} \ln\left(2\pi\sigma_o^2\right) - \frac{1}{2\sigma_o^2} \sum_{n=0}^{N-1} (Y[n] - g\,(n, m))^2\,. \quad (18)$$

Using the general CRLB for signals in AWGN [56] leads to

$$\mathrm{Var}[\hat{m}] \geq -\,\mathbf{E}\left[\frac{\partial^2 \ln p(\mathbf{Y}, m)}{\partial m^2}\right]^{-1}. \quad (19)$$

As the log-likelihood (18) is plugged into (19) and the first derivative w.r.t. the parameter m is carried out, it is

$$\frac{\mathrm{Var}[\hat{f}_c]}{\delta_f^2} \sum_{n=0}^{N-1} \left(\frac{\partial g(n, m)}{\partial m}\right)^2 \geq \sigma_o^2, \quad (20)$$

since $f_c = f_0 + m\delta_f$. The inequality (20) is true only if the likelihood $p(\mathbf{Y}, m)$ satisfies the regularity condition [56], which is $\mathbf{E}\,[\partial \ln p(\mathbf{Y}, m)/\partial m] = 0$, for $0 \leq m \leq N-1$. The condition is always satisfied since

$$\mathbf{E}\left[\frac{\ln\, \partial g(n, m)}{\partial m}\right] = \frac{1}{\sigma_o^2} \sum_{n=0}^{N-1} \frac{\partial g(n, m)}{\partial m}\, \mathbf{E}[Y[n] - g(n, m)] = 0, \quad (21)$$

as $\mathbf{E}[Y[n]] = X(f_0 + n\delta_f, f_0 + m\delta_f)$, thus the lower bound of the thesis (14) is proved.

APPENDIX G
PROOF OF COROLLARY 2 AND 3

Let $g(n, m) = g_0 + k_s|n - m|$, with $k_s \in \mathbb{R}$ and g_0 s.t. $g(n, m) \geq 0$, for $n \in [N_{g^-}, N_{g^+}]$, while $g(n, m) = 0$ elsewhere. Then, it is $|\partial g(n, m)/\partial m| = k_s$ for $n \in [N_{g^-}, N_{g^+}]$, and $|\partial g(n, m)/\partial m| = 0$ otherwise. Under this hypothesis, the right side of inequality (14) becomes $\sigma_o^2 \delta_f^2 / \sum_{n=0}^{N-1} (\partial g(n, m)/\partial m)^2 = \sigma_o^2 \delta_f^2 / \sum_{n=N_{g^-}}^{N_{g^+}} (\partial g(n, m)/\partial m)^2 = \sigma_o^2 \delta_f^2 / k_s^2 (N_{g^+} - N_{g^-})$, which proves the thesis (15). Corollary 3 follows when (14) is calculated for $g(n, m)$ Gaussian with mean $\mu_g = m\delta_f = f_c$ and variance σ_g^2, which leads to the thesis (16).

REFERENCES

[1] U. D. Ulusar, F. Al-Turjman, and G. Celik, "An overview of Internet of Things and wireless communications," in *Proc. Int. Conf. Comput. Sci. Eng. (UBMK)*, Oct. 2017, pp. 506–509.

[2] D. Wang, D. Chen, B. Song, N. Guizani, X. Yu, and X. Du, "From IoT to 5G I-IoT: The next generation IoT-based intelligent algorithms and 5G technologies," *IEEE Commun. Mag.*, vol. 56, no. 10, pp. 114–120, Oct. 2018.

[3] M. O. A. Kalaa, J. Guag, and S. J. Seidman, "An outlook on wireless coexistence with focus on medical devices," *IEEE Electromagn. Compat. Mag.*, vol. 7, no. 3, pp. 60–64, Oct. 2018.

[4] M. Gidlund, T. Lennvall, and J. Akerberg, "Will 5G become yet another wireless technology for industrial automation?" in *Proc. IEEE Int. Conf. Ind. Technol. (ICIT)*, Mar. 2017, pp. 1319–1324.

[5] R. Natarajan, P. Zand, and M. Nabi, "Analysis of coexistence between IEEE 802.15.4, BLE and IEEE 802.11 in the 2.4 GHz ISM band," in *Proc. 42nd Annu. Conf. IEEE Ind. Electron. Soc. (IECON)*, Oct. 2016, pp. 6025–6032.

[6] Y. Matsumoto, M. Takeuchi, K. Fujii, A. Sugiura, and Y. Yamanaka, "Performance analysis of interference problems involving DS-SS WLAN systems and microwave ovens," *IEEE Trans. Electromagn. Compat.*, vol. 47, no. 1, pp. 45–53, Feb. 2005.

[7] M. Lichtman, J. D. Poston, S. Amuru, C. Shahriar, T. C. Clancy, R. M. Buehrer, and J. H. Reed, "A communications jamming taxonomy," *IEEE Secur. Privacy*, vol. 14, no. 1, pp. 47–54, Jan. 2016.

[8] *AN1017: Zigbee and Silicon Labs Thread Coexistence With Wi-Fi*. Accessed: Nov. 29, 2019. [Online]. Available: www.silabs.com

[9] C. E. C. Bastidas, J. A. Stine, A. Rennier, M. Sherman, A. Lackpour, M. M. Kokar, and R. Schrage, "IEEE 1900.5.2: Standard method for modeling spectrum consumption: Introduction and use cases," *IEEE Commun. Standards Mag.*, vol. 2, no. 4, pp. 49–55, Dec. 2018.

[10] *IEEE Standard for Information Technology*, IEEE Standard 802.11-2016, Dec. 2016, pp. 1–3534.

[11] *Wireless Systems for Industrial Automation: Process Control and Related Applications*, document ISA 100.11a-2011, International Society of Automation, 2011.

[12] E. Sisinni, A. Saifullah, S. Han, U. Jennehag, and M. Gidlund, "Industrial Internet of Things: Challenges, opportunities, and directions," *IEEE Trans Ind. Informat.*, vol. 14, no. 11, pp. 4724–4734, Nov. 2018.

[13] *IEEE Standard for Definitions and Concepts for Dynamic Spectrum Access: Terminology Relating to Emerging Wireless Networks, System Functionality, and Spectrum Management—Redline*, IEEE Standard 1900.1-2019 (Revision IEEE Std 1900.1-2008), Apr. 2019, pp. 1–144.

[14] T. M. Chiwewe, C. F. Mbuya, and G. P. Hancke, "Using cognitive radio for interference-resistant industrial wireless sensor networks: An overview," *IEEE Trans Ind. Informat.*, vol. 11, no. 6, pp. 1466–1481, Dec. 2015.

[15] M. Hoyhtya, A. Mammela, M. Eskola, M. Matinmikko, J. Kalliovaara, J. Ojaniemi, J. Suutala, R. Ekman, R. Bacchus, and D. Roberson, "Spectrum occupancy measurements: A survey and use of interference maps," *IEEE Commun. Surveys Tuts.*, vol. 18, no. 4, pp. 2386–2414, 4th Quart., 2016.

[16] W. Liu, M. Kulin, T. Kazaz, A. Shahid, I. Moerman, and E. De Poorter, "Wireless technology recognition based on RSSI distribution at sub-nyquist sampling rate for constrained devices," *Sensors*, vol. 17, no. 9, p. 2081, Sep. 2017.

[17] Q. Zhao and B. M. Sadler, "A survey of dynamic spectrum access," *IEEE Signal Process. Mag.*, vol. 24, no. 3, pp. 79–89, May 2007.

[18] Metageek. *Wi-Spy Data Sheet*. Accessed: Nov. 29, 2019. [Online]. Available: https://www.support.metageek.com/

[19] V. Sokolov, A. Carlsson, and I. Kuzminykh, "Scheme for dynamic channel allocation with interference reduction in wireless sensor network," in *Proc. 4th Int. Sci.-Practical Conf. Problems Infocommun. Sci. Technol. (PIC S T)*, Oct. 2017, pp. 564–568.

[20] M. A. Taha, M. T. Abdallah, H. Al Qasem, and M. A. Sada, "Dynamic spectrum analyzer using software defined radio," in *Proc. Int. Conf. Interact. Mobile Comput. Aided Learn. (IMCL)*, Nov. 2012, pp. 167–172.

[21] C. Cordeiro, K. Challapali, D. Birru, and S. Shankar, "IEEE 802.22: The first worldwide wireless standard based on cognitive radios," in *Proc. 1st IEEE Int. Symp. New Frontiers Dyn. Spectr. Access Netw. (DySPAN)*, Nov. 2005, pp. 328–337.

[22] F. Mehmeti and T. Spyropoulos, "To scan or not to scan: The effect of channel heterogeneity on optimal scanning policies," in *Proc. IEEE Int. Conf. Sens., Commun. Netw. (SECON)*, Jun. 2013, pp. 264–272.

[23] H. Kim and K. G. Shin, "Fast discovery of spectrum opportunities in cognitive radio networks," in *Proc. 3rd IEEE Symp. New Frontiers Dyn. Spectr. Access Netw.*, Oct. 2008, pp. 1–12.

[24] S. Grimaldi, A. Mahmood, and M. Gidlund, "Real-time interference identification via supervised learning: Embedding coexistence awareness in IoT devices," *IEEE Access*, vol. 7, pp. 835–850, 2019.

[25] S. Grunau, D. Block, and U. Meier, "Multi-label wireless interference classification with convolutional neural networks," in *Proc. IEEE 16th Int. Conf. Ind. Informat. (INDIN)*, Jul. 2018, pp. 187–192.

[26] E. Axell, S. O. Tengstrand, and K. Wiklundh, "Online classification of class a impulse interference," in *Proc. IEEE Mil. Commun. Conf. (MILCOM)*, Oct. 2017, pp. 180–184.

[27] F. P. Rezha and S. Young Shin, "Performance analysis of ISA100.11a under interference from an IEEE 802.11b wireless network," *IEEE Trans Ind. Informat.*, vol. 10, no. 2, pp. 919–927, May 2014.

[28] Y. Serizawa, R. Fujiwara, T. Yano, and M. Miyazaki, "Reliable wireless communication technology of adaptive channel diversity (ACD) method based on ISA100.11a standard," *IEEE Trans. Ind. Electron.*, vol. 64, no. 1, pp. 624–632, Jan. 2017.

[29] V. Kotsiou, G. Z. Papadopoulos, D. Zorbas, P. Chatzimisios, and A. F. Theoleyre, "Blacklisting-based channel hopping approaches in low-power and lossy networks," *IEEE Commun. Mag.*, vol. 57, no. 2, pp. 48–53, Feb. 2019.

[30] L. Tytgat, O. Yaron, S. Pollin, I. Moerman, and P. Demeester, "Analysis and experimental verification of frequency-based interference avoidance mechanisms in IEEE 802.15.4," *IEEE/ACM Trans. Netw.*, vol. 23, no. 2, pp. 369–382, Apr. 2015.

[31] S. Grimaldi, M. Gidlund, T. Lennvall, and F. Barac, "Detecting communication blackout in industrial wireless sensor networks," in *Proc. IEEE World Conf. Factory Commun. Syst. (WFCS)*, May 2016, pp. 1–8.

[32] Tektronix. *Fundamentals of Real-time Spectrum Analysis—Primer, Tektronix*. Accessed: Mar. 2, 2020. [Online]. Available: https://www.tek.com/primer/fundamentals-real-time-spectrum-analysis

[33] V. Iglesias, J. Grajal, M. A. Sanchez, and M. Lopez-Vallejo, "Implementation of a real-time spectrum analyzer on FPGA platforms," *IEEE Trans. Instrum. Meas.*, vol. 64, no. 2, pp. 338–355, Feb. 2015.

[34] Q. Liu, M. Li, X. Kong, and N. Zhao, "Disrupting MIMO communications with optimal jamming signal design," *IEEE Trans. Wireless Commun.*, vol. 14, no. 10, pp. 5313–5325, Oct. 2015.

[35] L. Sujbert and G. Orosz, "FFT-based spectrum analysis in the case of data loss," in *Proc. IEEE Int. Instrum. Meas. Technol. Conf. (I2MTC)*, May 2015, pp. 800–805.

[36] A. Ali and W. Hamouda, "Advances on spectrum sensing for cognitive radio networks: Theory and applications," *IEEE Commun. Surveys Tuts.*, vol. 19, no. 2, pp. 1277–1304, 2nd Quart., 2017.

[37] *IEEE Standard for Low-Rate Wireless Networks*, IEEE Standard 802.15.4-2015, Apr. 2016, pp. 1–709.

[38] Y. Chen and A. Terzis, "On the mechanisms and effects of calibrating RSSI measurements for 802.15.4 radios," in *Proc. EWSN*, 2010, pp. 256–271.

[39] Texas Instruments. *2.4 GHz IEEE 802.15.4/ZigBee-Ready RF Transceiver*. Accessed: Nov. 29, 2019. [Online]. Available: www.ti.com

[40] F. M. Gardner, *Phaselock Techniques*, 3rd ed. Hoboken, NJ, USA: Wiley, 2005.

[41] R. Hemmecke, M. Köppe, J. Lee, and R. Weismantel, "Nonlinear integer programming," 2009, *arXiv:0906.5171*. [Online]. Available: http://arxiv.org/abs/0906.5171

[42] N. S. Alagha and P. Kabal, "Generalized raised-cosine filters," *IEEE Trans. Commun.*, vol. 47, no. 7, pp. 989–997, Jul. 1999.

[43] C. Liu and F. Li, "Spectrum modelling of OFDM signals for WLAN," *Electron. Lett.*, vol. 40, no. 22, pp. 1431–1432, Oct. 2004.

[44] E. Jacobsen and P. Kootsookos, "Fast, accurate frequency estimators [DSP tips & tricks]," *IEEE Signal Process. Mag.*, vol. 24, no. 3, pp. 123–125, May 2007.

[45] Ç. Candan, "A method for fine resolution frequency estimation from three DFT samples," *IEEE Signal Process. Lett.*, vol. 18, no. 6, pp. 351–354, Jun. 2011.

[46] Memsic. *TelosB Mote Platform Datasheet*. Accessed: Nov. 29, 2019. [Online]. Available: www.memsic.com

[47] F. Chiti, R. Fantacci, and A. Tani, "Performance evaluation of an adaptive channel allocation technique for cognitive wireless sensor networks," *IEEE Trans. Veh. Technol.*, vol. 66, no. 6, pp. 5351–5363, Jun. 2017.

[48] C.-F. Lindberg and A. J. Isaksson, "Comparison of different sampling schemes for wireless control subject to packet losses," in *Proc. Int. Conf. Event-based Control, Commun., Signal Process. (EBCCSP)*, Jun. 2015, pp. 1–8.
[49] National Instruments. *USRP-2921 Software Defined Radio Device*. Accessed: Nov. 29, 2019. [Online]. Available: www.ni.com
[50] M. Hamdaoui and P. Ramanathan, "A dynamic priority assignment technique for streams with (m, k)-firm deadlines," *IEEE Trans. Comput.*, vol. 44, no. 12, pp. 1443–1451, Dec. 1995.
[51] P. Park, P. D. Marco, and K. H. Johansson, "Cross-layer optimization for industrial control applications using wireless sensor and actuator mesh networks," *IEEE Trans. Ind. Electron.*, vol. 64, no. 4, pp. 3250–3259, Apr. 2017.
[52] T. Zhang, T. Gong, C. Gu, H. Ji, S. Han, Q. Deng, and X. S. Hu, "Distributed dynamic packet scheduling for handling disturbances in real-time wireless networks," in *Proc. IEEE Real-Time Embedded Technol. Appl. Symp. (RTAS)*, Apr. 2017, pp. 261–272.
[53] V. D. Barnett, "Order statistics estimators of the location of the cauchy distribution," *J. Amer. Stat. Assoc.*, vol. 61, no. 316, pp. 1205–1218, Dec. 1966.
[54] J. Hayya, D. Armstrong, and N. Gressis, "A note on the ratio of two normally distributed variables," *Manage. Sci.*, vol. 21, no. 11, pp. 1338–1341, Jul. 1975.
[55] D. E. Knuth, "Johann faulhaber and sums of powers," *Math. Comput.*, vol. 61, no. 203, p. 277, Sep. 1993.
[56] S. M. Kay, *Fundamentals of Statistical Signal Processing: Estimation Theory*. Upper Saddle River, NJ, USA: Prentice-Hall, 1993.

SIMONE GRIMALDI (Member, IEEE) received the B.Sc. and M.Sc. degrees in telecommunication engineering from the University of L'Aquila, L'Aquila, Italy, in 2010 and 2015, respectively. He is currently pursuing the Ph.D. degree with the Department of Information Systems and Technology, Mid Sweden University, Sweden. In 2015, he was an M.Sc. thesis worker with ABB Corporate Research, Västerås, Sweden. His current research interests include reliable wireless communication in harsh environments, interference management, and coexistence of wireless technologies.

LUKAS MARTENVORMFELDE received the B.Sc. degree in electrical engineering from the Ostwestfalen-Lippe University of Applied Sciences, Lemgo, Germany, in 2017, where he is currently pursuing the corresponding M.Sc. degree. He worked as a Student Research Assistant at the Institute Industrial IT (inIT), Lemgo, Germany. In 2019, he was a Research Intern at the Department of Information Systems and Technology, Mid Sweden University, Sundsvall, Sweden. His research interests include industrial communication systems with the focus on wireless technologies.

AAMIR MAHMOOD (Senior Member, IEEE) received the B.E. degree in electrical engineering from the National University of Sciences and Technology (NUST), Pakistan, in 2002, and the M.Sc. and D.Sc. degrees in communications engineering from the Aalto University School of Electrical Engineering, Finland, in 2008 and 2014, respectively. He worked as a Research Intern at the Nokia Researcher Center, Finland, in 2014, a Visiting Researcher at Aalto University, from 2015 to 2016, and also a Postdoctoral Researcher at Mid Sweden University (MIUN), Sweden, from 2016 to 2018. Since 2019, he has been an Assistant Professor with the Department of Information Systems and Technology, MIUN. His research interests include low-power local/wide-area networks, energy-delay aware radio resource allocation, and RF interference/coexistence management.

MIKAEL GIDLUND (Senior Member, IEEE) received the Lic. Eng. degree in radio communication systems from the KTH Royal Institute of Technology, Sweden, in 2004, and the Ph.D. degree in electrical engineering from Mid Sweden University, Sweden, in 2005. From 2008 to 2015, he was a Senior Principal Scientist and Global Research Area Coordinator of Wireless Technologies, ABB Corporate Research, Sweden. From 2007 to 2008, he was the Project Manager and the Senior Specialist with Nera Networks AS, Norway. From 2006 to 2007, he was a Research Engineer and also the Project Manager of Acreo AB, Sweden. Since 2015, he has been a Professor of computer engineering with Mid Sweden University. He holds more than 20 patents (granted and pending applications) in the area of wireless communication. His current research interests include wireless communication and networks, wireless sensor networks, access protocols, and security. He is an Associate Editor of the IEEE TRANSACTIONS ON INDUSTRIAL INFORMATICS.